



Permeability Evolution of Fractured Sorptive Geomaterials: A Theoretical Study on Coalbed Methane Reservoir

Xiang Zhou¹ · Shimin Liu² · Yida Zhang¹

Received: 17 August 2020 / Accepted: 9 February 2021 / Published online: 6 March 2021
© The Author(s), under exclusive licence to Springer-Verlag GmbH, AT part of Springer Nature 2021

Abstract

Fractured sorptive geomaterials (FSG) are ubiquitous in geological systems such as coal, shale and chalk. The solid matrix of FSG can adsorb species in gas or liquid form, the process of which is often accompanied by the deformation and microstructural alternation of the matrix. Such coupling is further obscured by the presence of fracture network, introducing complex fracture–matrix interactions. Predicting the hydromechanical properties of FSG is of particular importance for the production of coalbed methane (CBM) which requires the assessment of coal permeability under varying pressure and stress conditions. This study attempts to investigate the interplay between adsorption, deformation, and permeability evolution of coals. The novel concept of adsorption stress popularized in material science research is adopted here to construct a mechanistic theory describing sorption-induced deformation of coals. The constitutive theory is implemented in a finite element (FE) scheme and then adopted for describing coal matrix in a FE model of coal–fracture system. The model is calibrated for San Juan coals and applied to simulate a typical methane depletion test. It is observed that, depending on the competing effect between desorption-induced fracture opening and poroelastic compaction, the predicted permeability curve may be monotonically increasing (rising type) or decreasing (decline type), or may exhibit reduction first and then increase (rebound type) during gas depletion. Such competition is found to be controlled by the volume ratio, the permeability ratio, and the stiffness ratio between the matrix and the fracture elements. The prediction covers a wide range of permeability data obtained from laboratory tests and field observations.

Keywords Coal · Permeability evolution · Sorption-induced strain · Fracture–matrix interaction · Finite element modeling

List of Symbols

A_s	Lagrangian specific surface area	M	Molar mass of adsorptive species
$a_s, a_{s,0}$	Current and initial Eulerian specific surface area	N	Biot's modulus
B	Equilibrium constant of gas	n, n_0	Eulerian current and initial porosity
b	Biot's coefficient	P	Fluid pressure
C_n	Tangent of geometrical relation	P_a	Adsorption pressure
C_{ads}	Tangent of adsorption isotherm	\mathbf{q}_f	Fluid flux rate
\mathbf{E}	Green–Lagrangian strain	R	Gas content
E	Young's modulus	R_i	Inner radius of spherical pore
\mathbf{e}	Strain deviator	R_o	Outer radius of spherical pore
G	Shear modulus	\mathbf{S}	Second Piola–Kirchhoff stress
K	Bulk modulus	\mathbf{s}	Stress deviator
k, k_0	Current and initial permeability	S_s	Entropy of solid
		T	Absolute temperature
		\mathbf{u}	Displacement
		\mathbf{v}_s	Velocity
		Γ	Surface excess concentration
		Γ^{\max}	Maximum adsorption
		γ	Solid–fluid interfacial energy
		ΔR_i	Change of the pore radius
		$\boldsymbol{\varepsilon}$	Infinitesimal strain tensor

✉ Yida Zhang
yida.zhang@colorado.edu

¹ University of Colorado Boulder, Boulder, CO, USA

² Department of Energy and Mineral Engineering, G3 Center and Energy Institute, The Pennsylvania State University, University Park, PA 16802, USA

ε	Volumetric strain
ε_{11}	Horizontal strain
μ	Chemical potential
μ_d	Dynamic viscosity of fluid
ν	Poisson's ratio
Π	Gas adsorption amount
ρ	Mass density
$\boldsymbol{\sigma}$	Cauchy stress tensor
σ	Mean stress
σ_a	Adsorption stress
σ_h	Horizontal stress
σ_v	Vertical stress
σ^s	Surface stress
Ψ_s	Total Helmholtz free energy potentials of solid
ϕ, ϕ_0	Current and initial Lagrangian porosity

1 Introduction

Many subsurface geological materials are composed of adsorptive porous matrices intersected by natural fractures (e.g. coal, shale and chalk), which may be collectively referred to as fractured sorptive geomaterials (FSG). Compared with the classical notion of fractured rocks, the solid skeleton of FSG can have rich interactions with the saturating gas and/or formation liquid. Such interaction can be of chemical or physical nature and mainly serves as an additional storage mechanism (i.e. adsorption) of the fluid in the FSG matrices. For example, when injecting methane or CO₂ in coals, the gas molecules are not just filling the pore space but are also adsorbed onto the coal internal surface at a denser and structurally ordered state, termed as gas sorption. The ad-/de-sorption of gas molecules near the solid–fluid interface can alter its surface tension and cause the swelling/shrinkage of the solid matrix (Hol and Spiers 2012). Such a process is also known to change the pore structure and in turn affects the adsorption and the transport properties of the material (Harpalani and Schraufnagel 1990). Compared to engineered porous materials, FSG possesses one more layer of complexity—the fracture network. Natural fractures often have aperture size orders of magnitude larger than the size of pores with drastically different geometrical characteristics, thus modifying the coupled adsorption–deformation–transport behavior of the material by introducing compartmentalization, anisotropy, and other structural effects.

Predicting the hydromechanical properties of FSG is of particular importance in the production of coalbed methane (CBM). Methane transport during extraction is a multiscale process. First, the overall fluid pressure in the coalbed is reduced, accompanied by the desorption of methane molecules from pore surfaces. The detached molecules are then migrated through the coal matrix and micropores towards the nearest cleat or fracture. The flow of gas becomes

significantly eased in the natural cleat/fracture network, which can be described locally by slit flow or collectively by Darcy's law (Harpalani and Schraufnagel 1990). Accompanied by the desorption of methane, coal matrix exhibits notable volumetric shrinkage and changes of the pore structures (Zhang et al. 2016). The adsorption-induced strain combined with the in situ (uniaxial strain) boundary condition can widen the cleat and change the conductivity of the fracture network, impacting the overall permeability of the coal seam.

Various permeability models for such a system have been proposed. They may be roughly categorized into stress-based and strain-based models (Gu and Chalaturnyk 2006; Palmer 2009; Pan and Connell 2012). Stress-based models regard stress as the fundamental cause of permeability variation in coals (Cui and Bustin 2005; Gilman and Beckie 2000; Liu and Rutqvist 2010; Shi and Durucan 2004). They often involve a geomechanical model that predicts sorption-induced strain and the corresponding changes of horizontal stress. The stress change is then used to update the permeability via an exponential equation (Cui and Bustin 2005; Seidle et al. 1992; Shi and Durucan 2004). Porosity usually does not appear in the stress-based calculations, which is somewhat counter-intuitive (Palmer 2009). Strain-based models, on the other hand, attribute any permeability variation to the change of porosity and cleat width (Levine 1996; Liu et al. 2011; Ma et al. 2011; Palmer and Mansoori 1996; Seidle and Huitt 1995). The cubic law (Reiss 1980) is then called to compute the permeability. The aforementioned models have oversimplified the geomechanical aspect of the problem by avoiding dealing with the fundamental relations between adsorption strain, adsorption isotherm, pore microstructure and the mechanical properties of coal. By lumping all the underlying mechanisms in a single strain–pressure or porosity–pressure equation, these models cannot be physically generalized to different in situ processes relevant to CBM, including coupling between lithostatic stress and adsorption (Liu et al. 2016; Pone et al. 2009) and differential radial and axial swelling/shrinkage (Espinoza et al. 2013; Hol and Spiers 2012). Besides, both families implicitly assume that the Biot's coefficient equals unity, which is generally not correct for deep formations (Liu and Harpalani 2013).

Sorption-induced straining of a porous medium has recently attracted tremendous interest in the field of material science, driven by the development of new nanoporous materials like aerogel, biopolymers and metal–organic frameworks (MOFs). An important concept offered by these studies is the so-called adsorption stress derived from either macroscopic thermodynamics (Brochard et al. 2012; Coussy 2010; Nikoosokhan et al. 2014; Vandamme et al. 2010) or molecular computations (Gor et al. 2017; Gor and Neimark 2011; Ravikovitch and Neimark 2006). Adsorption stress

represents the additional stresses felt by an adsorptive porous skeleton compared to its inert or non-adsorptive counterpart. Such stress is originated from adsorbate–adsorbent interaction forces, and reflects the overall mechanical effect of guest molecules on the pore wall and further in deforming the porous medium (Gor et al. 2017; Gor and Neimark 2010; Vandamme et al. 2010; Zhang 2018). Adsorption stress has a sound micromechanical basis and can be directly computed from molecular simulations, thus enabling new capabilities for physics-based interpretation of various mechano-sorptive phenomena of porous materials. Thus far, the concept of adsorption stress has yet to be applied in understanding the hydromechanical response of FSGs.

The purpose of this study is, therefore, threefold: (1) introduce a poromechanics theory based on the concept of adsorption stress to describe the mechano-sorptive behavior of coal matrix (Sect. 3); (2) implement the theory in a finite element scheme with embedded fractures to represent general FSGs (Sect. 4); and (3) conduct coupled hydromechanical simulations to understand the impact of local shrinkage and matrix–fracture interaction on the apparent permeability of coals during methane depletion (Sect. 5). Results and possible future extensions of this study are discussed at the end (Sect. 6).

2 An Adsorptive Poroelastic Model Based on Adsorption Stress

One of the earliest rationalizations of adsorption-induced swelling is by Bangham and his co-workers (Bangham and Fakhoury 1928; Bangham and Razouk 1938): adsorption reduces surface energy of the solid–fluid interfaces, leading to the relaxation of the solid skeleton which causes the macroscopic expansion of the porous media. Such effect is now referred to as the Bangham effect. Thermodynamic theories (Coussy 2010; Vandamme et al. 2010) have been proposed to incorporate the effect of solid–fluid surface energy in modeling the mechanics of sorptive porous materials. Adsorption stress is naturally derived from such theory as the macroscopic stress conjugated to the swelling strain. Recently, Zhang (2018) has rigorously derived the free energy balance equation proposed in Vandamme et al. (2010) from the fundamental balance laws of individual phases, thus confirming the adsorption stresses are not constitutive hypothesis but are natural results of energy conservation of the system. The theory deals with a saturated porous representative elementary volume (REV) and treats the solid–fluid interface as an independent phase that can carry mass, energy and entropy. The balance laws of each phase are written following the formalism of mixture theory (Coussy et al. 1998). The derived Clausius–Duhem inequality embodies the coupled fluid, species and heat conduction

laws, the state equations of the fluid mixture, the Gibb’s isotherm, and the free energy imbalance of the solid skeleton (Zhang 2018). The last item serves as the starting point for constitutive modeling of sorptive porous media:

$$\mathbf{S} : d\mathbf{E} + Pd\phi - S_s dT - \sigma^s dA_s - d\Psi_s \geq 0, \tag{1}$$

where Ψ_s is the Helmholtz free energy of the solid phase; \mathbf{S} is the Second Piola–Kirchhoff stress; \mathbf{E} is the Green–Lagrangian strain; P is fluid pressure; ϕ is the Lagrangian porosity; S_s is solid entropy; T the absolute temperature; A_s is the specific surface area per unit reference volume; σ^s is the surface stress (Shuttleworth 1950) which becomes identical to the familiar notion of solid–fluid interfacial energy γ (or surface tension) if neglecting surface stretch. Eq. (1) can be simplified by considering reversible, isothermal and infinitesimal deformation process:

$$d\Psi_s = \sigma d\epsilon + \mathbf{s} : d\mathbf{e} + Pd\phi - \gamma dA_s, \tag{2}$$

where ϵ is the linearized strain tensor; $\epsilon = \text{tr}(\mathbf{e})$ and $\mathbf{e} = \boldsymbol{\epsilon} - \text{tr}(\boldsymbol{\epsilon})\mathbf{I}/3$ are the volumetric strain and strain deviator, respectively; $\sigma = \text{tr}(\boldsymbol{\sigma})/3$ and $\mathbf{s} = \boldsymbol{\sigma} - \text{tr}(\boldsymbol{\sigma})\mathbf{I}/3$ are the mean stress and stress deviator, respectively. Comparing to the free energy balance of a non-reactive porous solid (Coussy 2004), the specific surface area A_s now enters the macroscopic Ψ -potential, thus permitting the surface properties affects the thermomechanical response of the porous solid.

Proposing Ψ_{ss} in the form of $\Psi_s(\epsilon, \mathbf{e}, \phi)$ and substituting into Eq. (2), the hyperelastic relation for an adsorptive porous medium can be obtained as:

$$\sigma - \sigma_a = \left. \frac{\partial \Psi_s}{\partial \epsilon} \right|_{\phi, \mathbf{e}} ; P - P_a = \left. \frac{\partial \Psi_s}{\partial \phi} \right|_{\epsilon, \mathbf{e}} ; \mathbf{s} = \left. \frac{\partial \Psi_s}{\partial \mathbf{e}} \right|_{\epsilon, \phi}, \tag{3}$$

where

$$\sigma_a = \gamma \left. \frac{\partial A_s}{\partial \epsilon} \right|_{\phi, \mathbf{e}} ; P_a = \gamma \left. \frac{\partial A_s}{\partial \phi} \right|_{\epsilon, \mathbf{e}}, \tag{4}$$

are the previously discussed *adsorption stresses* that modify the stresses felt by the skeleton as shown in Eq. (3). These stresses produce an overall compressive pre-stress on the porous media even in the apparent stress-free condition. Equations (3) and (4) contain all the information needed to define an elastic model for adsorptive porous media. Constitutive choices are reflected through the expression of the Helmholtz free energy $\Psi_s(\epsilon, \mathbf{e}, \phi)$, the geometrical relation $A_s = A_s(\epsilon, \phi)$, and the surface energy $\gamma(\epsilon_A, \mu)$ where ϵ_A is the surface strain and μ is the chemical potential of adsorptive species. This reveals a unique advantage of this framework: the various mechanisms contributing to adsorption–deformation can be decoupled with their interrelations clearly delineated (Fig. 1), offering numerous opportunities for material-specific adaptations and applications. Below

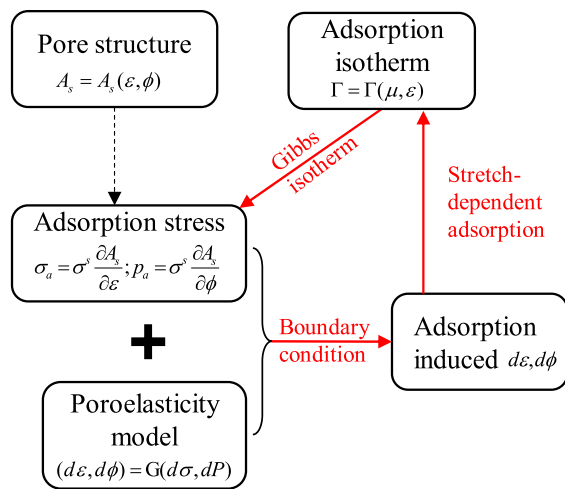


Fig. 1 Structure of the adsorptive poromechanics theory of Zhang (2018). The red arrows highlight the mechanisms involved in the two-way coupling between adsorption and straining

we specialize a simple constitutive model describing coal matrix under unary gas adsorption.

The simplest poroelastic model is the linear isotropic one. The corresponding free energy potential Ψ_s has the following expression (Coussy 2004):

$$\Psi_s(\varepsilon, \mathbf{e}, \phi) = \frac{1}{2}(K + b^2N)\varepsilon^2 - bN\varepsilon(\phi - \phi_0) + \frac{1}{2}N(\phi - \phi_0)^2 + G\mathbf{e} : \mathbf{e}, \quad (5)$$

where K and G are bulk and shear modulus, respectively; b and N are Biot's coefficient and Biot's modulus, respectively. Substituting Eq. (5) into (3) gives the explicit constitutive relations:

$$\begin{aligned} \sigma - \sigma_a &= (K + b^2N)\varepsilon - bN(\phi - \phi_0) \\ P - P_a &= -bN\varepsilon + N(\phi - \phi_0) \\ \mathbf{s} &= 2G\mathbf{e}. \end{aligned} \quad (6)$$

On the microstructure aspect, considering a coal matrix with monosized spherical pores, the initial and the current porosity can be computed by the following (Zhang 2018):

$$\phi_0 = \frac{R_i^3}{R_o^3}; \phi = \frac{(R_i + \Delta R_i)^3}{R_o^3}, \quad (7)$$

where R_i is the inner and R_o is the outer radius of the sphere; ΔR_i is the change of the pore radius. A_s can be similarly expressed after eliminating R_o and ΔR_i using Eq. (7):

$$A_s = \frac{3(R_i + \Delta R_i)^2}{R_o^3} = \frac{3}{R_i} \phi_0^{1/3} \phi^{2/3}. \quad (8)$$

The structural factors can be immediately derived:

$$\left. \frac{\partial A_s}{\partial \varepsilon} \right|_{\phi, \mathbf{e}} = 0; \left. \frac{\partial A_s}{\partial \phi} \right|_{\varepsilon, \mathbf{e}} = \frac{2}{R_i} \left(\frac{\phi_0}{\phi} \right)^{1/3}. \quad (9)$$

Finally, the simplest adsorption model for unary gas adsorption is the Langmuir model.

$$\Gamma = \frac{\Gamma^{\max}BP}{1 + BP} \text{ or } \rho_{\text{surf}} = \frac{M\Gamma^{\max}BP}{1 + BP}, \quad (10)$$

where Γ is the surface excess concentration with a unit of mole/area; Γ^{\max} and B are adsorption parameters corresponding to the specific gas and solid surface; M is the molar mass of adsorptive species. The surface energy can be finally derived by integrating the Gibbs adsorption isotherm $d\gamma = -\Gamma d\mu$ (DeHoff 2006) combined with Eq. (10) and $d\mu = RTd(\ln P)$:

$$\Delta\gamma = \gamma - \gamma_0 = -RT \int_0^P \Gamma(P)d \ln P = -RT\Gamma^{\max} \ln(1 + BP), \quad (11)$$

where $R = 8.314$ J/mol K is the ideal gas constant. Equations (4), (6), (9) and (11) completes the basic isotropic adsorption-swelling model which will be used to describe coal matrix in this study. Note that the current formulation only

captures the one-way coupling of adsorption-induced deformation. The impact of deformation on the sorption capacity of coals is not captured because the adsorption isotherm Eq. (10) and the derived surface tension Eq. (11) are independent of surface stretch in the current model. Incorporating such two-way coupling is important in revealing the effect of lithostatic stress on CBM production (Liu et al. 2016). This non-trivial task is beyond the current scope and will be pursued in follow-up studies.

3 Finite Element Solution for A-HM Problems

This section solves the field equations depicting gas transport in a deformable porous medium via a user-defined element subroutine (UEL) in the finite element (FE) package ABAQUS for adsorptive hydromechanical (A-HM) problems. The benefit of this approach is having the freedom of using any user-specific constitutive models for the adsorptive matrix and full control over the fracture geometry in simulating generic FSGs, and at the same time

taking advantage of the robust nonlinear solver offered by ABAQUS.

3.1 Governing Equations

Given an arbitrary domain with volume Ω_t and boundary $\partial\Omega_t$, the time rate of change of quantity ξ of the α phase must be equal to the source/sink rate \dot{r}_ξ subtract the net outflux. This can be written as

$$\frac{D^\alpha}{Dt} \int_{\Omega_t} \xi dV = \int_{\Omega_t} \frac{\partial \xi}{\partial t} dV + \int_{\partial\Omega_t} (\xi \mathbf{v}_\alpha) \cdot \mathbf{n} dA = \int_{\Omega_t} \dot{r}_\xi dV, \tag{12}$$

where

$$\frac{D^\alpha}{Dt}(\cdot) = \frac{\partial}{\partial t}(\cdot) + \mathbf{v}_\alpha \cdot \nabla_x(\cdot) \tag{13}$$

is the particle derivative of a field with respect to the α phase; \mathbf{v}_α is the velocity of the α phase; $\nabla_x(\cdot)$ denotes gradient operation with respect to spatial coordinate; $\alpha = s$ for the solid, f for the fluid and surf for the surface phase. Letting the interested quantity ξ be the fluid mass per unit volume $n\rho_f$ where n is the Eulerian porosity, the fluid mass balance can be expressed as

$$\frac{D^f}{Dt} \int_{\Omega_t} (n\rho_f) dV = \int_{\Omega_t} \dot{r}_f dV. \tag{14}$$

Letting ξ be the surface adsorption per unit volume $\rho_{\text{surf}}a_s$, the solid–fluid interface can be regarded as an independent phase obeying its own mass balance law:

$$\frac{D^{\text{surf}}}{Dt} \int_{\Omega_t} (\rho_{\text{surf}}a_s) dV = \int_{\Omega_t} \dot{r}_{\text{surf}} dV, \tag{15}$$

where a_s is the Eulerian specific surface area; ρ_{surf} is the surface mass density. In the current development, the source/sink terms for the fluid and the surface phases \dot{r}_f and \dot{r}_{surf} are solely due to mass exchange between the two due to adsorption/desorption. Thus, we have $\dot{r}_f = -\dot{r}_{\text{surf}} = \dot{r}$. Substituting this relation and applying the Reynold transport theorem and divergence theorem on Eqs. (14) and (15) gives

$$\frac{\partial(n\rho_f)}{\partial t} + \nabla_x \cdot (n\rho_f \mathbf{v}_f) = \dot{r}, \tag{16}$$

$$\frac{\partial(\rho_{\text{surf}}a_s)}{\partial t} + \nabla_x \cdot (\rho_{\text{surf}}a_s \mathbf{v}_{\text{surf}}) = -\dot{r}. \tag{17}$$

For FE implementation, it is necessary to express Eqs. (16) and (17) in terms of particle derivatives with respect to the solid phase (also called the material time derivative) using Eq. (13):

$$\frac{D^s}{Dt} (n\rho_f) - \mathbf{v}_s \cdot \nabla_x (n\rho_f) + \nabla_x \cdot (n\rho_f \mathbf{v}_f) = \dot{r}, \tag{18}$$

$$\frac{D^s}{Dt} (\rho_{\text{surf}}a_s) - \mathbf{v}_s \cdot \nabla_x (\rho_{\text{surf}}a_s) + \nabla_x \cdot (\rho_{\text{surf}}a_s \mathbf{v}_{\text{surf}}) = -\dot{r}. \tag{19}$$

It is possible to write $\mathbf{v}_{\text{surf}} = \mathbf{v}_s$ by assuming the surface phase moves along with solid skeleton. For conciseness, we also replace the operator $D^s \xi / Dt$ by $\dot{\xi}$ and the spatial gradient ∇_x by ∇ hereafter. Considering the above, Eqs. (18) and (19) can be finally written as follows:

$$\rho_f \dot{n} + n \dot{\rho}_f + (n\rho_f) \nabla \cdot \mathbf{v}_s + \nabla \cdot \mathbf{q}_f = \dot{r}, \tag{20}$$

$$\rho_{\text{surf}} \dot{a}_s + a_s \dot{\rho}_{\text{surf}} + \rho_{\text{surf}} a_s \nabla \cdot \mathbf{v}_s = -\dot{r}, \tag{21}$$

where \mathbf{q}_f is the fluid mass flux vector defined by

$$\mathbf{q}_f \equiv \rho_f n (\mathbf{v}_f - \mathbf{v}_s). \tag{22}$$

According to Darcy’s law, \mathbf{q}_f is related to pressure gradient by

$$\mathbf{q}_f = -\frac{\rho_f k}{\mu_d} (\nabla P - \rho_f \mathbf{g}), \tag{23}$$

where μ_d is the dynamic viscosity of fluid; k is the permeability; \mathbf{g} is the gravitational acceleration vector.

Equations (20) and (21) are the mass balance equations for the fluid and the surface phases, respectively. We note that the surface mass density ρ_{surf} is related with the fluid pressure via adsorption isotherm Eq. (10); a_s is related to Eulerian porosity via the geometrical relation Eq. (8) (under the small strain assumption $a_s \approx A_s$, $\phi \approx n$); $\nabla \cdot \mathbf{v}_s$ is essentially the volumetric strain rate $\dot{\epsilon}$; and fluid compressibility can be taken into account by replacing $\partial\rho_f/\partial P$ with ρ_f/P for ideal gases. Substituting these relations and summing Eqs. (20) and (21), the total mass balance equation for the adsorptive species in the system can be obtained as

$$(\rho_{\text{surf}}C_n + \rho_f)\dot{n} + \left(a_s C_{\text{ads}} + n \frac{\rho_f}{P}\right)\dot{P} + (\rho_{\text{surf}}a_s + \rho_f n)\dot{\epsilon} + \nabla \cdot \mathbf{q}_f = 0, \tag{24}$$

where C_n and C_{ads} are the tangents of the geometrical relation and the adsorption isotherm, respectively. Under small strain assumption, their expressions can be obtained from Eqs. (8) and (10):

$$C_n = \frac{\partial a_s}{\partial n} = \frac{2}{R_i} \left(\frac{n_0}{n}\right)^{1/3}, \tag{25}$$

$$C_{\text{ads}} = \frac{\partial \rho_{\text{surf}}}{\partial P} = \frac{M\Gamma_{\text{max}}B - M\Gamma_{\text{max}}B^2P}{(1 + BP)^2}. \tag{26}$$

3.2 Implementation

The governing equations of our system include the mass balance Eq. (24) and the mechanical equilibrium condition:

$$\nabla \cdot \boldsymbol{\sigma} = 0. \tag{27}$$

For the mechanical part, let $\partial\Omega_u$ and $\partial\Omega_t$ be complementary subsurface of boundary $\partial\Omega$ of the volume Ω in the sense $\partial\Omega = \partial\Omega_u \cup \partial\Omega_t$ and $\partial\Omega_u \cap \partial\Omega_t = \emptyset$. Then for a time interval $t \in [0, T]$, we consider a pair of boundary conditions where the displacement \mathbf{u} is prescribed on $\partial\Omega_u$ and traction on $\partial\Omega_t$. The initial condition is taken as

$$\mathbf{u}(\mathbf{x}, 0) = \mathbf{u}_0(\mathbf{x}). \tag{28}$$

Similarly for the hydraulic aspect, assuming $\partial\Omega_f^P$ and $\partial\Omega_f^k$ be complementary subsurface of boundary $\partial\Omega$ of the volume Ω in the sense $\partial\Omega = \partial\Omega_f^P \cup \partial\Omega_f^k$ and $\partial\Omega_f^P \cap \partial\Omega_f^k = \emptyset$. Then for a time interval $t \in [0, \Delta t]$, we consider a pair of boundary conditions where the fluid pressure P is prescribed on $\partial\Omega_f^P$ and flux on $\partial\Omega_f^k$. The initial condition is taken as

$$P(\mathbf{x}, 0) = P_0(\mathbf{x}). \tag{29}$$

The initial porosity of the system can be set as n_0 everywhere. Combining the governing equations and boundary condition defined above, the strong form of the PDEs describing fully coupled A-HM problem are

- M (mechanical)

$$\left\{ \begin{array}{l} \nabla \cdot \boldsymbol{\sigma} = 0 \text{ in } \Omega \\ \mathbf{u} = \tilde{\mathbf{u}} \text{ on } \partial\Omega_u \times [0, \Delta t] \\ \boldsymbol{\sigma}\mathbf{n} = \tilde{\mathbf{t}} \text{ on } \partial\Omega_t \times [0, \Delta t] \end{array} \right\}. \tag{30}$$

- H (hydraulic)

$$\left\{ \begin{array}{l} (\rho_{\text{surf}}C_n + \rho_f)\dot{n} + \left(a_s C_{\text{ads}} + n \frac{\rho_f}{P}\right)\dot{P} + (\rho_{\text{surf}}a_s + \rho_f n)\dot{\epsilon} + \nabla \cdot \mathbf{q}_f = 0 \text{ in } \Omega \\ P = \tilde{P}_f \text{ on } \partial\Omega_f^P \times [0, \Delta t] \\ \mathbf{q}_f \mathbf{n} = \tilde{q}_f^k \text{ on } \partial\Omega_f^k \times [0, \Delta t] \end{array} \right\}. \tag{31}$$

Introducing weighting functions $\mathbf{w}_1, \mathbf{w}_2$ that vanish on $\partial\Omega_u$ and $\partial\Omega_f^P$, respectively, the corresponding weak forms are

- M:

$$\int_{\Omega} \frac{\partial \mathbf{w}_1}{\partial \mathbf{x}} \boldsymbol{\sigma} d\Omega = \mathbf{w}_1 \tilde{\mathbf{t}}. \tag{32}$$

- H:

$$\int_{\Omega} w_2 (\rho_{\text{surf}}C_n + \rho_f)\dot{n} d\Omega + \int_{\Omega} w_2 \left(a_s C_{\text{ads}} + n \frac{\rho_f}{P}\right)\dot{P} d\Omega + \int_{\Omega} w_2 (\rho_{\text{surf}}a_s + \rho_f n)\dot{\epsilon} d\Omega + w_2 \tilde{q}_f^k - \int_{\Omega} \mathbf{q}_f \cdot \nabla w_2 d\Omega = 0. \tag{33}$$

The standard Galerkin method where the weighting fields share the same shape function for interpolation inside each element is employed for spatial discretization:

- M: with $\mathbf{u} = \mathbf{N}\tilde{\mathbf{u}}$ and $\mathbf{w}_1 = \mathbf{N}\tilde{\mathbf{w}}_1$, $\tilde{\mathbf{u}}$ is the nodal displacements.

$$\int_{\Omega} \mathbf{B}^T \boldsymbol{\sigma}(\mathbf{u}) d\Omega - \mathbf{N}^T \tilde{\mathbf{t}} = 0. \tag{34}$$

- H: with $P = \mathbf{N}\tilde{P}$ and $w_2 = \mathbf{N}\tilde{w}_2$, \tilde{P} is the array of nodal pressure.

$$\int_{\Omega} \mathbf{N}^T (\rho_{\text{surf}}C_n + \rho_f)\dot{n} d\Omega + \int_{\Omega} \mathbf{N}^T \left(a_s C_{\text{ads}} + n \frac{\rho_f}{P}\right)\dot{P} d\Omega + \int_{\Omega} \mathbf{N}^T (\rho_{\text{surf}}a_s + \rho_f n)\dot{\epsilon} d\Omega + \mathbf{N}^T \tilde{q}_f^k - \int_{\Omega} (\nabla \mathbf{N})^T \mathbf{q}_f d\Omega = 0, \tag{35}$$

where

$$\mathbf{B} = \frac{\partial \mathbf{N}}{\partial \mathbf{x}} = \begin{bmatrix} \frac{\partial N_1}{\partial x} & 0 & 0 & \frac{\partial N_2}{\partial x} & 0 & 0 & \dots & \frac{\partial N_n}{\partial x} & 0 & 0 \\ 0 & \frac{\partial N_1}{\partial y} & 0 & 0 & \frac{\partial N_2}{\partial y} & 0 & \dots & 0 & \frac{\partial N_n}{\partial y} & 0 \\ 0 & 0 & \frac{\partial N_1}{\partial z} & 0 & 0 & \frac{\partial N_2}{\partial z} & \dots & 0 & 0 & \frac{\partial N_n}{\partial z} \\ 0 & \frac{\partial N_1}{\partial z} & \frac{\partial N_1}{\partial y} & 0 & \frac{\partial N_2}{\partial z} & \frac{\partial N_2}{\partial y} & \dots & 0 & \frac{\partial N_n}{\partial z} & \frac{\partial N_n}{\partial y} \\ \frac{\partial N_1}{\partial z} & 0 & \frac{\partial N_1}{\partial y} & \frac{\partial N_2}{\partial z} & 0 & \frac{\partial N_1}{\partial y} & \dots & \frac{\partial N_n}{\partial z} & 0 & \frac{\partial N_n}{\partial y} \\ \frac{\partial N_1}{\partial y} & \frac{\partial N_1}{\partial x} & 0 & \frac{\partial N_2}{\partial y} & \frac{\partial N_1}{\partial x} & 0 & \dots & \frac{\partial N_n}{\partial y} & \frac{\partial N_n}{\partial x} & 0 \end{bmatrix}. \tag{36}$$

The system of coupled equations is solved by the Newton–Raphson method, where the elemental Jacobian $\mathbf{K} = \mathbf{A}\mathbf{M}\mathbf{A}^T\mathbf{R}\mathbf{X}$ and the residual $\mathbf{R} = \mathbf{R}\mathbf{H}\mathbf{S}$ are required to solve the nodal unknowns for n integration points at each iteration attempt:

$$\underbrace{\begin{bmatrix} \mathbf{K}_{uu}^{t+\Delta t} & \mathbf{K}_{uP}^{t+\Delta t} \\ \mathbf{K}_{Pu}^{t+\Delta t} & \mathbf{K}_{PP}^{t+\Delta t} \end{bmatrix}}_{\mathbf{A}\mathbf{M}\mathbf{A}^T\mathbf{R}\mathbf{X}} \begin{bmatrix} \delta \tilde{\mathbf{u}} \\ \delta \tilde{P} \end{bmatrix} = \underbrace{\begin{bmatrix} -\mathbf{R}_M^{t+\Delta t} \\ -\mathbf{R}_H^{t+\Delta t} \end{bmatrix}}_{\mathbf{R}\mathbf{H}\mathbf{S}}. \tag{37}$$

According to the discretized weak form given in the last section, the residual $[R]$ at $t + \Delta t$ step can be defined below:

$$R_M^{t+\Delta t} = - \int_{\Omega} \mathbf{B}^T \boldsymbol{\sigma}(\mathbf{u}^{t+\Delta t}) d\Omega - \mathbf{N}^T \tilde{\mathbf{t}}, \tag{38}$$

$$R_H^{t+\Delta t} = - \int_{\Omega} \mathbf{N}^T (\rho_{\text{surf}} C_n + \rho_f) \dot{n} d\Omega - \int_{\Omega} \mathbf{N}^T \left(a_s C_{\text{ads}} + n \frac{\rho_f}{p^{t+\Delta t}} \right) \dot{p} d\Omega - \int_{\Omega} \mathbf{N}^T (\rho_{\text{surf}} a_s + \rho_f n) \dot{\epsilon} d\Omega - \mathbf{N}^T \tilde{q}_f^k + \int_{\Omega} (\nabla \mathbf{N})^T \mathbf{q}_f d\Omega. \tag{39}$$

The final expressions of Jacobian and numerical integral form of $[R]$ and $[K]$ are summarized in Appendix A. They are then coded in the UEL subroutine to be used together with the ABAQUS Standard solver to achieve monolithic solution of A-HM problems.

4 Verification

Hereafter we specialize the above FE scheme for modeling coal–methane systems. By way of verifying the implementation of the A-HM UEL, two types of simulations are conducted, the first one simulates a single-element test and the second one considers a single coal column subjected to methane depletion.

4.1 Single Element Test

Single element test is a necessary step to verify the correct implementation of the constitutive model in the UEL before applying it to large-scale boundary value problems with thousands of elements. Here a single element model representing coal specimen is subjected to unjacketed gas pressurization test (Hol and Spiers 2012), i.e. increasing total stress and pore pressure from 0 to 10 MPa. All six surfaces are free to move with total compressive stress equal to the pore gas pressure during pressurization. The constitutive model described in Sect. 3 is separately implemented into a stand-alone Matlab driver and subjected to the same stress path. The computed swelling strain and methane adsorption from the A-HM UEL and the Matlab driver are plotted together in Fig. 2. Methane adsorption Π_{CH_4} is defined as the number of moles of methane adsorbed on coal matrix per gram, which is related to surface excess Γ_{CH_4} via $\Pi_{\text{CH}_4} = \Gamma_{\text{CH}_4} a_{s,0} / \rho_s (1 - n_0)$ where $a_{s,0}$ and n_0 represent initial specific surface area and porosity, respectively. It is observed that results from the UEL and the stand-alone constitutive driver match exactly in terms of both variables, thus verifying the implementation of the constitutive equations. One can see that the predicted swelling strain has a similar trend as the Langmuir adsorption isotherm. This is because the adsorption stress in Eq. (4) is originated from the surface

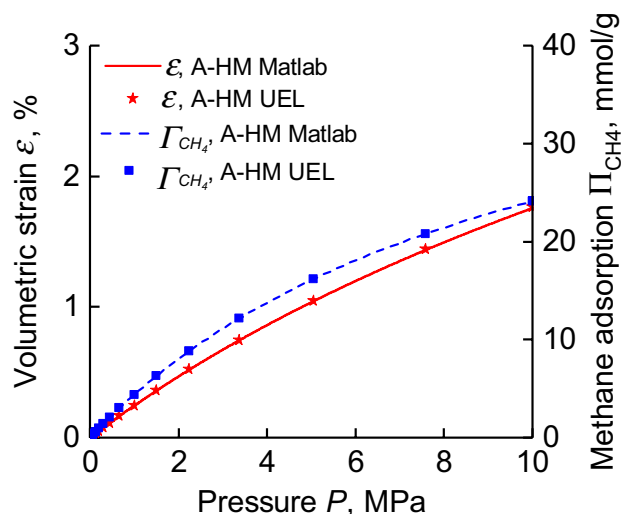


Fig. 2 Predicted adsorption and swelling isotherms from a standalone constitutive driver and a single-element A-HM UEL simulation. Parameters used: $G=2.95$ GPa, $K=2.7$ GPa, $n_0=0.1$, $b=0.9$, $R_i = 1$ nm, $\Gamma_{\text{CH}_4}^{\text{max}} = 1.5 \times 10^{-5}$ mol/m², $B_{\text{CH}_4} = 1 \times 10^{-7}$, $\mu = 1 \times 10^{-5}$ Pa s

tension Eq. (10) which is integrated from the adsorption isotherm.

4.2 Porous Column Test

To examine the model performance in capturing coupled diffusion–adsorption–deformation process, we consider an initially pressurized ($P = 5$ MPa) coal-only column under one-dimensional (1D) methane depletion. One end of the column is considered as the fracture surface, thus has a lower gas pressure ($P = 1$ MPa) and is free to move. The rest of the boundaries are undrained and fixed in the normal direction. The mesh and the boundary conditions are shown in Fig. 3. During the simulation, the pressure on the fracture boundary drops from 5 to 1 MPa in 1000 s and then maintained constant for 1×10^6 s. Parameters used here are identical with single element test. The permeability k is set as 1 mD.

The predicted pressure and volumetric strain profiles along the column at different time points are presented in Fig. 3. It shows that, at the early stage of depletion ($t = 10^4$ s), the majority of the region is still in the initial pressure and strain state except for a sharp gradient extending by around 1 mm away from the fracture surface. The volumetric strain is negative in this range, indicating that shrinkage occurred due to the depletion and desorption of methane. As diffusion continues ($t = 10^5$ s), the depletion and shrinkage fronts propagate to about 6 mm into the coal matrix. At the end of the simulation ($t = 10^6$ s), these fronts have reached the end of the column and all elements experience some degree of gas pressure reduction and volumetric shrinkage. Note that the coupled processes of diffusion, desorption and shrinkage

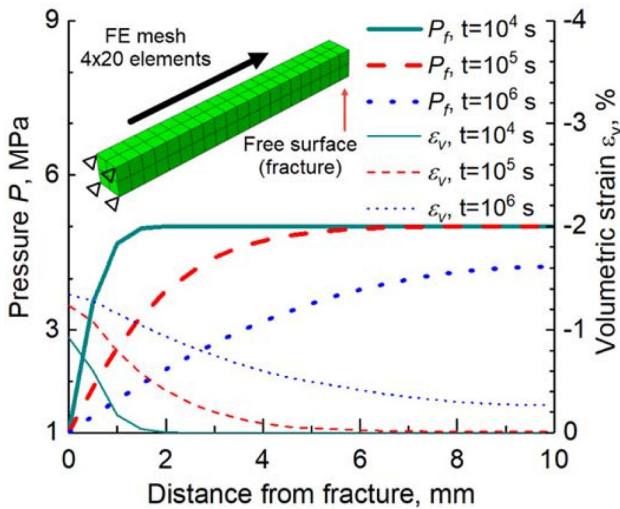


Fig. 3 Distribution of P and ε along the coal column at different times (10^4 s, 10^5 s, 10^6 s)

occur simultaneously thanks to the monolithic solution provided by the ABAQUS + UEL scheme.

Figure 4 plots the displacement history of the fracture surface, showing a total of 0.07 mm displacement accumulated due to the shrinkages of the coal matrices. In field condition, this translates to an opening up of the fracture which is the reason for the apparent permeability increase during CBM production. The subfigure in Fig. 4 presents the contour of methane adsorption at the end ($t = 10^6$ s). It is apparent that the coal near the free surface (fracture) contains much less methane due to lower pore gas pressure, thus nicely visualizing the degree of depletion across the column.

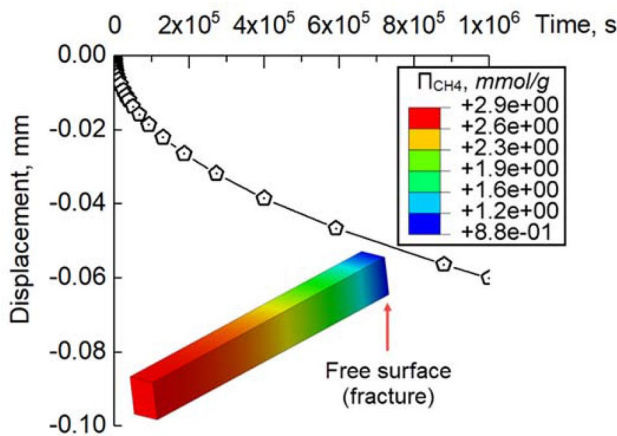


Fig. 4 Time history of the end displacement and contour of methane adsorption (mmol/g) at $t = 10^6$ s

5 Model Performance

5.1 FE Model and Parameter Calibration for San Juan CBM Reservoir

We select the dataset by Liu and Harpalani (2014a, b) for calibration and testing the predictive capability of the proposed theory. Their experiments measured the strain and stress evolutions under gas depletion for laterally constrained coal samples from San Juan basin. Under the best replicated in situ geomechanical conditions, the overburden stress was maintained at a constant value of 14.5 MPa, with initial horizontal stress at around 9.6 MPa. The reservoir temperature was estimated to be 35 °C and the initial pore gas pressure was 7.6 MPa. Depletion tests were carried out in a stepwise manner, reducing the gas pressure from 7.6 to 0.7 MPa in six steps. Two types of gases, helium and methane, each representing the non-sorptive and sorptive gases respectively, were used as the saturating gases in the tests. Zero horizontal strain ε_{11} was always ensured by adjusting horizontal stress throughout the test. The resultant horizontal stress and volumetric strain were reported after attaining equilibrium at each step. Such dataset offers comprehensive information about the poroelastic and adsorption properties of the specimen and is ideal for model calibration purposes.

Coal is characterized by a dual-porosity network with the macro-porosity mainly contributed by a fracture network that consists of face and butt cleats and bedding planes (Fig. 5), while the micro-porosity is contributed by the coal matrices (Dawson and Esterle 2010; Harpalani and Chen 1995). A simplified two-dimensional (2D) plane strain model with intersecting face and bedding fractures is adopted here as illustrated in Fig. 5. Such idealization is chosen to illustrate the most basic mechanisms governing the permeability evolution of coal seams without the interference of geometrical complexity. The domain is discretized by 41×41 elements, representing a sample in the size of 40 mm \times 40 mm. The ratio between the width of coal matrix (D_c) and the fracture (D_f), as shown in Fig. 5, is chosen as 1000:1 in the baseline

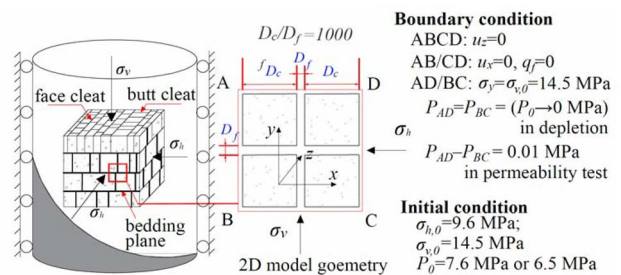


Fig. 5 Schematic of coal structure and idealization of 2D plane strain analysis

simulations. All nodal displacements are constrained in the out-of-plane (z) direction. The lateral boundaries are horizontally constrained to ensure the uniaxial strain condition as prescribed in the experiments.

Parameters for the coal matrix constituent are calibrated using the following procedure. First, the typical ranges of poroelastic and adsorption parameters of natural coals are identified from the existing literature. Most studies reported a range of Poisson's ratio ν between 0.25 and 0.4 and Young's modulus E_c between 0.85 and 3 GPa (Durucan and Shi 2009; Liu and Harpalani 2013; Palmer and Mansoori 1996; Shi and Durucan 2005; Shi et al. 2014; Shovkun and Espinoza 2017; Wang et al. 2014) for natural coals. Biot coefficient can be taken from 0.8 to 0.98 (Shovkun and Espinoza 2017; Zhao et al. 2003), sometimes even arguably larger than unity (Fan and Liu 2018). Constrained by these reported ranges, the poroelastic parameters of San Juan basin coal are determined by matching the horizontal stress and volumetric strain vs. pressure data from helium depletion tests reported in Liu and Harpalani (2014a, b), as shown, respectively, in Fig. 6a and b. Since helium is an inert gas considered as non-sorbing gas, the resultant strains during depletion solely reflect the poroelastic properties of the coal specimen

without the interference of mechano-sorptive effect. The adsorption parameters are determined by matching the methane adsorption isotherm of San Juan basin coal reported in Reeves (2001) and Wang and Liu (2016) as shown in Fig. 6c. The pore radius R_i for San Juan coal is approximately 1 nm according to Liu et al. (2019). Using these parameters and an initial porosity of $n_{0,c}=0.02$, the volumetric strain of San Juan basin coal under methane depletion is predicted in Fig. 6d. The result agrees exceptionally well with the measured data by Liu and Harpalani (2014a), thus validating model as well as the selected parameters in representing the mechano-sorptive behaviors of San Juan basin coals. Finally, the transport properties of the coal matrix have to be estimated because most studies only report the overall apparent permeability of coal specimens. Wang et al. (2013) measured the permeability of intact coal from 0.0007 to 0.06 mD, thus a value of 0.05 mD is used here. Table 1 summarizes all parameters for coal matrix used in the FE simulation.

The fractures in between coal matrices in Fig. 5 are simulated using finite-thickness continuum elements but with different material parameters than the coal matrix. By definition, fractures are empty spaces which should have negligible stiffness with little resistance to fluid flow. However,

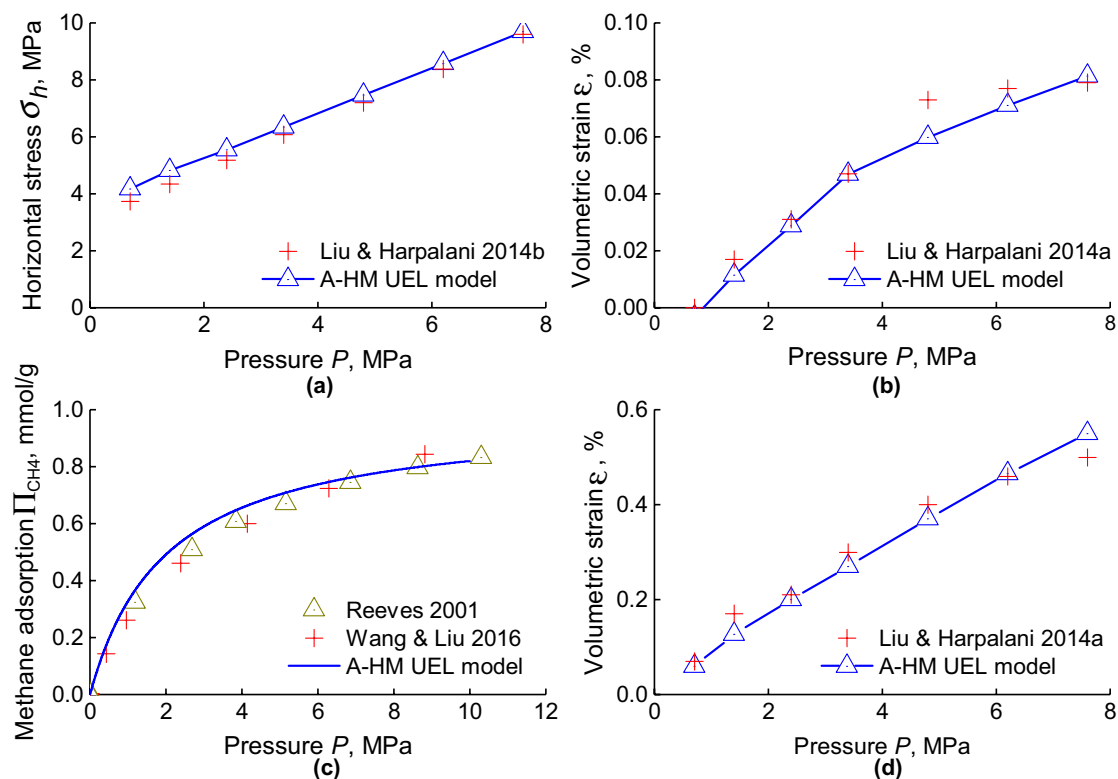


Fig. 6 Measured and modeled **a** horizontal stress during helium depletion (Liu and Harpalani 2014b), **b** volumetric strain during helium depletion (Liu and Harpalani 2014a), **c** methane adsorption isotherm (Reeves 2001; Wang and Liu 2016), and **d** volumetric strain

during methane depletion (Liu and Harpalani 2014a) for San Juan basin coal. The reference state with volumetric strain $\epsilon=0$ is set at vacuum condition where $P=0$ MPa

natural fractures often contain many asperities that resist normal and shear loadings. The aperture variations and the tortuous geometry of natural fractures also impose some degree of resistance to gas transport. Therefore, the continuum fracture elements are assigned a relatively small value of stiffness $E_f=6.48$ MPa and a relatively large initial permeability of $k_{f,0}=5$ mD compared to those of the coal matrix ($E_c/E_f=1000$, $k_{f,0}/k_{c,0}=100$). Adsorption in fractures is neglected by setting $\Gamma_{\text{CH}_4}^{\text{max}}=0$ for fracture elements. The rest of the parameters of the fracture elements are set the same as those of the coal matrix.

5.2 Permeability Updates for Coal and Fracture Elements

Gas flow in both coal matrix and cleat is described by Darcy's law Eq. (23) equipped with different permeability laws. The ability of the system in permeating gas flow strongly depends on the porosity of the coal matrix and the aperture of the cleat/fracture. Therefore, each type of element must be specified with a sound permeability–porosity or permeability–aperture relation to be coupled with the A-HM simulation to reflect such physics. For the coal matrix, the evolution of the permeability ratio $k_c/k_{c,0}$ can be described by the Kozeny–Carman equation which is derived based on laminar flow through a packed bed of solids (Kozeny 1927):

$$\frac{k_c}{k_{c,0}} = \frac{n_c^3}{n_{c,0}^3} \frac{(1 - n_{c,0})^2}{(1 - n_c)^2}, \quad (40)$$

or its simplified form (cubic law):

$$\frac{k_c}{k_{c,0}} = \frac{n_c^3}{n_{c,0}^3}, \quad (41)$$

where n_c and $n_{c,0}$ denote current and initial cleat porosity, respectively. On the other hand, fluid flow through a slit with an aperture h can be described by a quadratic relation assuming laminar flow through parallel plates (Sarkar et al. 2004):

$$\frac{k_f}{k_{f,0}} = \left(\frac{h}{h_0} \right)^2, \quad (42)$$

where k_f and $k_{f,0}$ are the current and initial permeability the fracture, respectively. Equations (41) and (42) are used to update the permeabilities of coal matrix and fracture in the simulations hereafter.

5.3 Transient Patterns During Continuous Gas Depletion

The calibrated model is now put to simulate the permeability evolution of San Juan basin coals during methane depletion. The numerical experiments are designed with reference to the laboratory tests by Mitra et al. (2012) and field observations by Clarkson et al. (2010). Mitra et al. (2012) conducted permeability tests on methane-saturated San Juan basin coal specimens with initial pore pressure of 6.2 MPa, using the same experimental setup as Liu and Harpalani (2014a, b). Clarkson et al. (2010) compute the gas relative permeability of the San Juan basin reservoir whose initial pore pressure is taken as 6.5 MPa during methane depletion based on the production data analysis technique. To compare with these two datasets, methane depletion tests are conducted on the FE model by reducing the initial pressure 6.5 MPa to final pressure 0.7 MPa in six steps. Each step consists of two parts: the first part reduces the gas pressure at the top and bottom boundaries to the target value and waits until equilibrium; the second part imposes a small pressure difference ($\Delta P=0.01$ MPa) between the top and bottom boundaries to measure the permeability of the matrix–fracture system. Figure 7 shows the imposed gas pressure at the boundaries and the resultant volumetric strain of the entire specimen. The reference state with volumetric strain $\varepsilon=0$ is set at the vacuum condition $P=0$ MPa. It is observed that the specimen shrinks (reduction of volumetric strain) rapidly after each reduction of pore pressure. The rate of change slows down and eventually the strain ceases evolving after equilibrium is attained. With the adopted parameters (Table 1), the model estimates about 30 days to complete the methane depletion test, which is comparable to the time span of real lab tests.

Figure 8 presents the snapshots of the spatial distribution of various quantities during depletion and permeability measurement at times t_1 , t_2 and t_3 as marked in Fig. 7.

Table 1 A-HM model parameters for coal matrix in FE simulation

Type	Property	Symbol	Value	Unit
Poroelasticity	Young's modulus	E_c	6.48	GPa
	Poisson's ratio	ν	0.1	
	Biot modulus	N	3.0×10^5	MPa
	Biot coefficient	b	0.9	
Adsorption	Maximum adsorption	$\Gamma_{\text{CH}_4}^{\text{max}}$	2.25×10^{-5}	mol/m ²
	Equilibrium constant	B_{CH_4}	5.0×10^{-8}	
	Temperature	T	315	K
	Gas content	R	8.314	J/K/mol
Transport	Intrinsic permeability	$k_{c,0}$	0.05	mD
	Dynamic viscosity	μ_d	1.2×10^{-5}	Pa s
Others	Initial porosity	$n_{0,c}$	0.02	
	Pore radius	R_i	1.0	nm
	Solid density	ρ_s	1.4×10^3	kg/m ³
	Fluid density	ρ_f	0.657	kg/m ³

Fig. 7 Imposed pressure history and observed strain history during methane depletion simulation

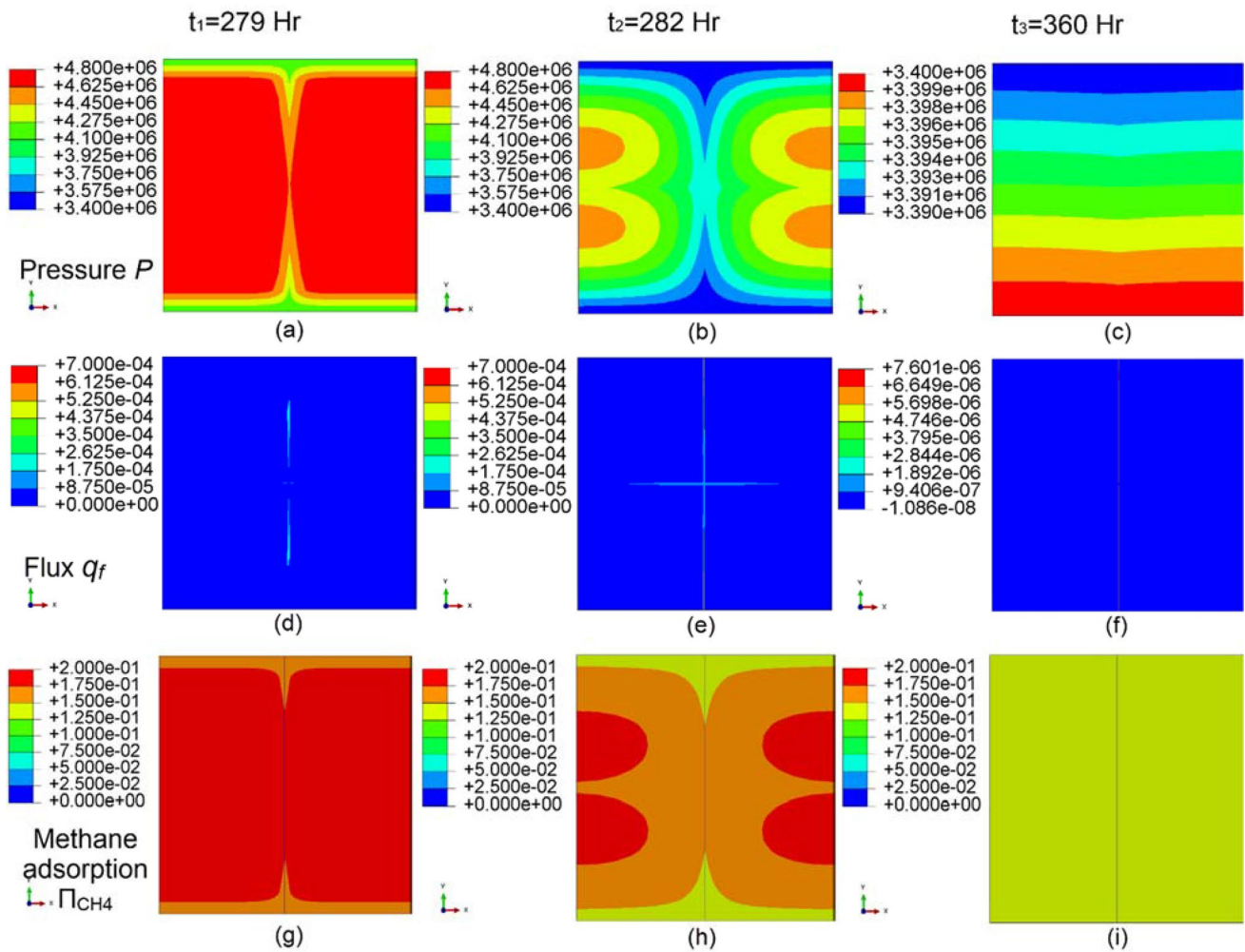
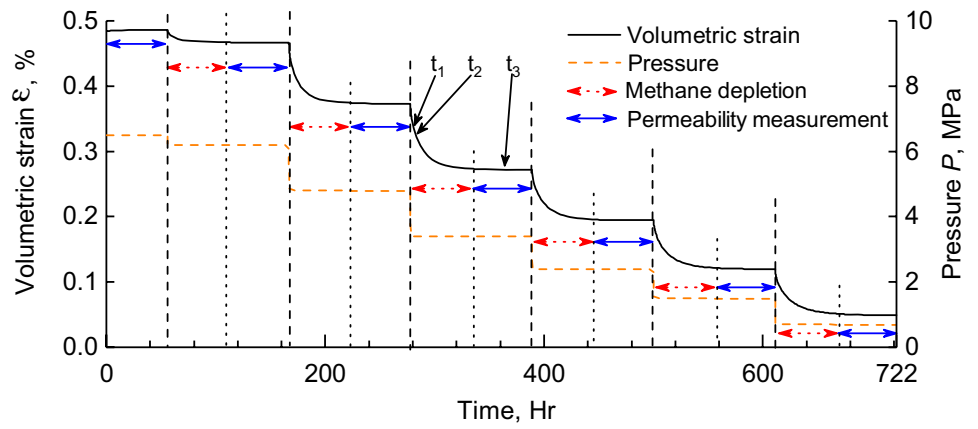


Fig. 8 Contours of fluid pressure P (a–c); net flux q_f (d–f); methane adsorption Π_{CH_4} (g–i) during methane depletion (t_1 , t_2) and permeability measurement (t_3)

Specifically, the contours of pressure P , net flux $q_f = \sqrt{q_{f,x}^2 + q_{f,y}^2}$, methane adsorption Π_{CH_4} are, respectively, presented in Fig. 8a–i. It is observed that at t_1 , shortly after pressure reduction being applied on top and bottom boundaries, methane has already started escaping from the coal matrix and the internal pressure field is already perturbed (Fig. 8a). Evidence of methane desorption and vertical flow can be also seen in Fig. 8d and g. Later at t_2 , pressure reduction (Fig. 8b) and methane desorption (Fig. 8h) have spread across a much wider region. It is observed that, due to the high permeability of the fracture elements, matrices adjacent to the horizontal fractures also exhibit large extent of desorption than the inner regions, creating a collective horizontal flow leading to the vertical fracture (Fig. 8e) even though the lateral boundaries are undrained. At t_3 during permeability test, pressure gradient is almost uniformly established in the specimen as depicted by Fig. 8c. Driven by such gradient, gas flow is developed predominantly in the vertical fractures (Fig. 8f). Permeability test is a steady-state test with small pressure gradients and therefore no new desorption is introduced (Fig. 8i).

Partially extracted from the full FE domain, Fig. 9 plots the horizontal strain along a horizontal path encompassing the matrix–fracture–matrix elements after attaining equilibrium at different pressures. The fracture element is aligned at $x=0$ in the x -axis. It is observed that, as the gas pressure decreases from 6.5 to 0.7 MPa, the widening of the fracture can reach about 150% which means 2.5 times its initial aperture size. The opening up of the fracture is due to the desorption-induced matrix shrinkage (i.e. negative strain) which can be seen in the zoomed-in subplot of Fig. 9. Such shrinkage causes the reduction of horizontal total and effective stresses and thus the widening of the fracture aperture.

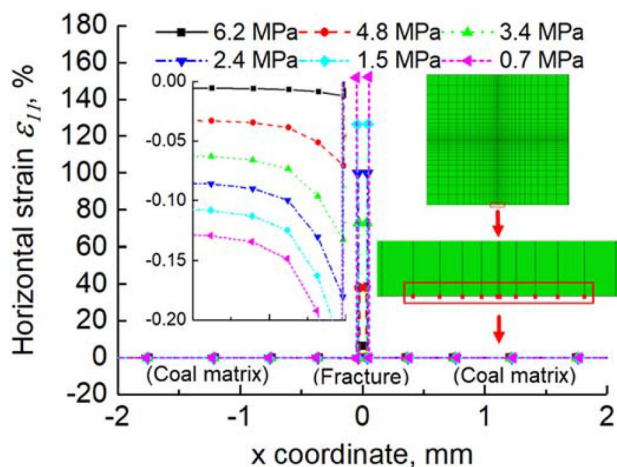


Fig. 9 Horizontal strain ε_{11} across the specimen during methane depletion

The desorption-induced coal matrix shrinkage and the resultant fracture opening up is the principle mechanism of permeability increasing of coalbeds during CBM (Harpalani and Chen 1997; Levine 1996), which will be quantitatively examined in the next section. It should be noted that desorption-induced widening only happens to the vertical crack because of the constant lateral strain boundary (Fig. 5). The horizontal crack, on the other hand, is actually predicted to have reduced aperture during depletion. This is due to the poroelastic compaction of the fracture element in the horizontal crack caused by the reduction of pore pressure. The shrinkage of coal matrix will not play any role in the horizontal fracture since the AD and BC boundaries (Fig. 5) can freely move to maintain a constant vertical total stress σ_v . This observation implies that the type of boundary condition is important in deducing the consequences of methane depletion in coal-fracture systems.

5.4 Permeability Evolution of the Overall Specimen

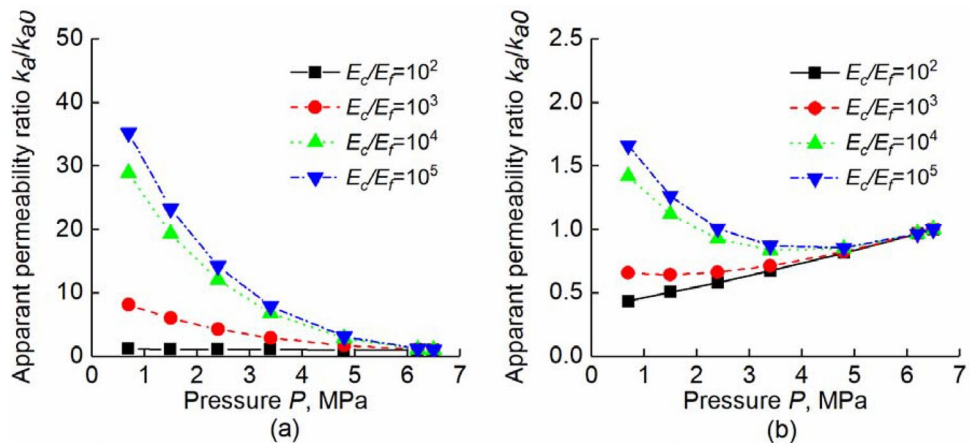
By treating the entire domain as a black box and interpreting the overall flow rate–pressure gradient data through Darcy’s law, the FE model can be used to study the evolution of the apparent permeability of coal seams during methane depletion and its sensitivity to various material properties. Denoting the width of i th coal matrix element as a_i and j th fracture element size as b_j , and their corresponding flux rates, respectively, as q_i and q_j , the total flux rate across the overall specimen can be assessed by:

$$q_{\text{total}} = \frac{\sum a_i q_i + \sum b_j q_j}{\sum a_i + \sum b_j} \quad (43)$$

The apparent permeability k_a can then be obtained via Darcy’s law $k_a = q_{\text{total}} \mu_d / \nabla P$. Each stage in Fig. 7 offers one k_a vs. P data point and thus a full permeability evolution curve can be obtained after each completed simulation.

In the previous baseline simulations, we have adopted a ratio of $E_c/E_f = 1000$ and $k_{f,0}/k_{c,0} = 100$ for the fracture element. It is, however, difficult to quantify the permeability and stiffness of fractures $k_{f,0}$ and E_f from direct laboratory tests and therefore to justify these parameter selections. Therefore, a parametric study is performed by perturbing the values of E_f and k_f to better understand their impacts on the predicted permeability evolution curves. The results of eight depletion simulations are summarized in Fig. 10. It is observed that for a high permeability ratio $k_{f,0}/k_{c,0} = 1000$ (Fig. 10a), where fracture serves as the main pathway for gas transport, methane depletion results in a monotonically increasing overall permeability of the system. The magnitude of permeability boost due to methane desorption is greater with the increasing stiffness ratio (E_c/E_f). This is expected since the more compliant the fracture is, the easier

Fig. 10 Relative permeability evolution under different stiffness ratios with **a** $k_{f,0}/k_{c,0} = 1000$ and **b** $k_{f,0}/k_{c,0} = 20$. The reference apparent permeability k_{a0} is taken at the initial condition $P = 6.5$ MPa



for it to open up due to the shrinkage of the adjacent coal matrices. Such effect becomes less obvious for stiffness ratio larger than 10^4 . This is because the permeability increase is ultimately bounded by how much the matrix can shrink rather than how compliant the fracture is.

Similarly, higher stiffness ratio is predicted to give higher permeability boost when a relatively low permeability ratio $k_{f,0}/k_{c,0} = 20$ is used (Fig. 10b). In this case, the fracture and the matrix are equally important in controlling the system’s apparent permeability. It is also observed that in this case, the apparent permeability decreases first at the early stage of depletion, then increases at lower pressure levels (i.e. the “V” shape of permeability evolution). Inspecting the simulation details shows that the shrinkage of the coal matrix at the beginning of pressure reduction is not significant enough to cause a substantial opening up of the fracture. This is because the desorption of gas at the beginning of depletion (around 3–6 MPa) is quite gradual (see Fig. 6c). Compaction of the bulk coal and reduction of matrix porosity, therefore, dominate the permeability evolution at the beginning of depletion. As gas pressure continues reducing to 1–3 MPa, the desorption process is accelerated and the induced shrinkage strain becomes sufficiently large to widen the fracture, thus causing the rebounding of the overall permeability of the coal-fracture system. For very low stiffness ratios (e.g. $E_c/E_f = 10^2$), permeability rebounding is never predicted, giving a monotonic decrease in apparent permeability as gas pressure reduces. This is because the stiffer the fractures the harder for the matrix shrinkage to cause any significant change on the fracture aperture. The permeability evolution of the entire system is, therefore, dominated by the reduction of matrix porosity caused by the poroelastic effect and thus exhibits a monotonic decreasing trend. Indeed, permeability change during CBM production is not always monotonically increasing. By monitoring 17 wells daily production drilled in Qinshui Basin of China, Chen et al. (2015) categorizes relative permeability curves into “rising type”, “decline type” and “rebound type”, which exactly correspond to 3

curving tendencies observed in this parametric study. It is worth highlighting that the proposed A-HM framework captures the different types of permeability curve only via adjusting physically meaningful parameters, thanks to its ability in resolving the intrinsic constitutive response of sorptive coal matrix and explicitly accounting for the fracture network.

Since permeability evolution is controlled by the relative straining of coal and fracture elements, the geometrical spacing ratio D_c/D_f (Fig. 5) could also be a critical factor in the predicted permeability curves. Ramandi et al. (2016) inspected the cleat network of coal sample obtained from the Bowen Basin in Australia via micro-CT imaging and scanning electron microscopy (SEM). They have measured a cleat spacing ranges from 1.2 mm ($D_{c,min}$) to 6.5 mm ($D_{c,max}$). Similarly using SEM and optical microscope, Bandyopadhyay et al. (2020) studied the cleat size distribution of coal samples from Raniganj Formation in Eastern India and reported the average aperture varies between 12 μm ($D_{f,min}$) and 49 μm ($D_{f,max}$). This gives a spacing ratio of 24 ($D_{c,min}/D_{f,max}$) to 542 ($D_{c,max}/D_{f,min}$). Taking the variability of coal formations into consideration, the range of $D_c/D_f = 10\text{--}1000$ may conservatively bound the matrix–fracture spacing ratios of natural coals. We, therefore, perform blind predictions on permeability evolution curves of specimens with two extreme spacing ratios ($D_c/D_f = 10:1$ and $1000:1$) using the baseline parameters listed in Table 1.

Simulation results for these two geometries are plotted in Fig. 11 together with field data (Clarkson et al. 2010) and laboratory data (Mitra et al. 2012) for San Juan basin coals. It is observed that permeability could increase by more than 20 times after depletion when fracture size is relatively small compared to bulk coal ($D_c/D_f = 1000:1$). On the contrary, permeability enhancement is not obvious for highly fractured specimens ($D_c/D_f = 10:1$). Indeed, the predicted curves enclose the field and laboratory data, visually offering an upper and lower bound for the range of permeability evolution for San Juan basin coals. This result suggests that the

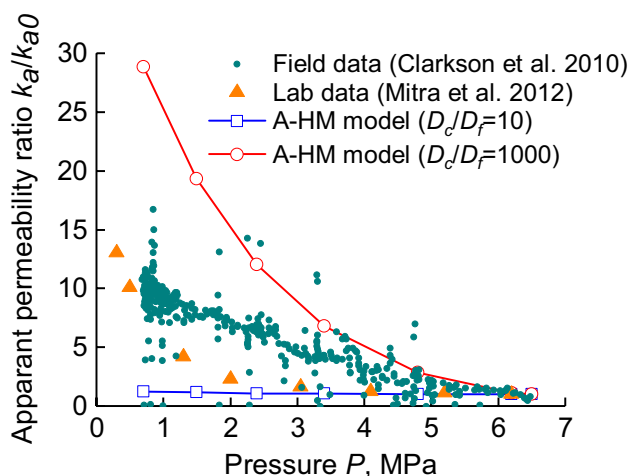


Fig. 11 Predicted relative permeability of San Juan coal under different space ratios ($D_c/D_f=10$ and 1000) vs. field data (Clarkson et al. 2010) and lab data (Mitra et al. 2012)

realistic average spacing ratio D_c/D_f should lie somewhere between 10 and 1000, which is supported by the aforementioned observations by Ramandi et al. (2016) and Bandyopadhyay et al. (2020). To further narrow down the predicted bounds and offer improved estimation of the permeability evolution curves, better characterization of the coal seams regarding its fracture network and spatial heterogeneity is desired.

6 Conclusions

A poromechanics theory describing sorption-induced deformation of sorptive porous media is developed based on the concept of adsorption stress. The theory decomposes the contribution of adsorption characteristics, poromechanical properties and pore geometry on the resultant adsorption-deformation behaviors, offering physics-based modeling of the mechano-sorptive behavior of porous materials. The model is then specialized for coal matrixes assuming Langmuir adsorption isotherm, linear poroelasticity, and spherical pores. The performance of the model is validated against methane and helium pressurization data on San Juan basin coals. Incorporation of the model in studying the hydromechanical behavior of FSGs is achieved through a novel finite element scheme that solves the coupled A-HM governing equations. By representing fracture via continuum element in a dual-porosity system, characteristics of coalbed methane reservoir such as matrix shrinkage, cleat opening up, porosity change, methane desorption during depletion can be simultaneously modeled. The coal matrix and fracture elements are assigned with different constitutive equations and permeability laws, which allows for predicting the evolution

of the fractured coal system under arbitrary stress and pressure paths to reflect in situ conditions. The main conclusions of this study are highlighted below:

1. Coupled A-HM simulations confirm that two competing effects, namely, poroelastic compaction and sorption-induced matrix shrinkage, control the permeability evolution of coals during methane depletion. In our proposed numerical model, the mechanosorptive response of coal matrix, the material heterogeneity, and the boundary conditions are separately accounted for, which provides a detailed mechanism-based quantification of their relative roles for permeability evolution.
2. Parametric study shows that the characteristics of permeability curve are controlled by the properties of the coal matrix and the fracture network, i.e. the volume ratio, the permeability ratio and the stiffness ratio between the matrix and the fracture elements.
3. By considering a matrix–fracture volume ratio of 10:1 and 1000:1 with representative coal parameters, the predicted permeability curves reasonably bound the permeability data from laboratory tests and field observations during CBM production. The model, therefore, predicts an intrinsic linkage between the cleat spacing and pressure-dependent dynamic permeability, which can provide guidance for future field application of this model based on petrographical data.

The modeling scheme offers the first of its kind to take the fracture/cleat spacing, in situ stress condition, and the matrix sorptive property to predict the apparent permeability evolution of coals. The proposed framework can be readily extended for describing coal seams in CBM or enhanced coalbed methane productions. First of all, the theory can incorporate adsorption of gas mixtures by replacing the fluid equation Eq. (39) by mole balance equation of each species combined with the extended Langmuir model (Zhang 2018). This is particularly useful for describing the adsorption–deformation behavior of coals in CO_2 -enhanced CBM production where the preferable adsorption of CO_2 over CH_4 on pore surfaces drives the methane production. Second, coal matrix is known to be anisotropic with respect to its bedding plane (Liu et al. 2020). The isotropic assumption adopted in this study may have oversimplified the calibration of the poroelastic properties of San Juan basin coals, which explains the relatively low value of the calibrated Poisson's ratio $\nu=0.1$ (Table 1). Incorporating anisotropy in the poroelastic description of coal matrix is expected to yield more realistic model parameters and better predictions on the resultant stress and strain response of coal specimens. Finally, the representation of the fracture network is drastically simplified in this study. It is envisaged that more realistic representation of the fracture network based

on observations from X-ray micro-tomography or scanning electron microscope (SEM) images can allow for a more systematic investigation of fracture–matrix interactions.

The validated modeling framework in this study demonstrates its ability to define the complex permeability behavior for the sorptive coal. The predicted permeability evolution can be coupled into the available commercial reservoir simulators, including CMG-GEM, ARI-COMET3D, IHS-F.A.S.T-CBM, to forecast the production profiles. Thus, the proposed model can serve as a bridge to link the petrographical properties into the reservoir flow model, which lays a foundation for mechanism-based reservoir modeling. Certainly, this study does not decompose the diffusion behavior of gas in micro- and macro-pores, instead, it takes an equivalent matrix permeability as a surrogate for diffusion coefficient. An improvement is required in the future study to incorporate pore-scale diffusion into the apparent permeability model.

Appendix A: Implementation Details of the A-HM UEL

Jacobian

In addition to residuals, the Jacobian terms in Eq. (37) are also required by the iterative solver which uses the Newton Rapson scheme. For conciseness, notation $t + \Delta t$ will be omitted, thus all kinematics and state variables are referred at the current time ($t + \Delta t$).

First, recalling Eq. (38), the Jacobian for the M equation can be derived as

$$\mathbf{K}_{uu} = -\frac{\partial R_M}{\partial \tilde{\mathbf{u}}} = \frac{\partial \int_{\Omega} \mathbf{B}^T \boldsymbol{\sigma} d\Omega}{\partial \tilde{\mathbf{u}}} = \int_{\Omega} \mathbf{B}^T \frac{\partial \boldsymbol{\sigma}}{\partial \tilde{\mathbf{u}}} d\Omega. \tag{44}$$

Considering $\mathbf{u} = \tilde{\mathbf{N}}\tilde{\mathbf{u}}$, we have $\frac{\partial \mathbf{u}}{\partial \tilde{\mathbf{u}}} = \mathbf{N}$, then $\frac{\partial \boldsymbol{\sigma}}{\partial \tilde{\mathbf{u}}} = \frac{\partial \boldsymbol{\sigma}}{\partial \boldsymbol{\varepsilon}} \frac{\partial \boldsymbol{\varepsilon}}{\partial \mathbf{u}} \frac{\partial \mathbf{u}}{\partial \tilde{\mathbf{u}}} = \mathbf{D}_{mm} \nabla_s \mathbf{N} = \mathbf{D}_{mm} \mathbf{B}$, thus

$$\mathbf{K}_{uu} = \int_{\Omega} \mathbf{B}^T \mathbf{D}_{mm} \mathbf{B} d\Omega, \tag{45}$$

where

$$\begin{aligned} \mathbf{K}_{Pu} &= \frac{1}{\Delta t} \int_{\Omega} \mathbf{N}^T (\rho_{\text{surf}} a_s + \rho_f n) J^{-1} \mathbf{D}_{nm} \mathbf{B} d\Omega + \int_{\Omega} \mathbf{N}^T \rho_{\text{surf}} \dot{n} \frac{\partial C_n}{\partial n} J^{-1} \mathbf{D}_{nm} \mathbf{B} d\Omega \\ &+ \int_{\Omega} \mathbf{N}^T \frac{\rho_f}{P} J^{-1} \mathbf{D}_{nm} \mathbf{B} \dot{P} d\Omega + \int_{\Omega} \mathbf{N}^T C_n C_{\text{ads}} J^{-1} \mathbf{D}_{nm} \mathbf{B} \dot{P} d\Omega \\ &+ \frac{1}{\Delta t} \int_{\Omega} \mathbf{N}^T (\rho_{\text{surf}} a_s + \rho_f n) \nabla^T \mathbf{N} d\Omega + \int_{\Omega} \mathbf{N}^T \rho_{\text{surf}} \dot{\varepsilon} C_n J^{-1} \mathbf{D}_{nm} \mathbf{B} d\Omega + \int_{\Omega} \mathbf{N}^T \rho_f \dot{\varepsilon} J^{-1} \mathbf{D}_{nm} \mathbf{B} d\Omega. \end{aligned} \tag{48}$$

$$\mathbf{D}_{mm} = \frac{\partial \boldsymbol{\sigma}}{\partial \boldsymbol{\varepsilon}} = \begin{bmatrix} K + \frac{4}{3}G & K - \frac{2}{3}G & K - \frac{2}{3}G & & & \\ K - \frac{2}{3}G & K + \frac{4}{3}G & K - \frac{2}{3}G & & & \\ K - \frac{2}{3}G & K - \frac{2}{3}G & K + \frac{4}{3}G & & & \\ & & & 2G & & \\ & & & & 2G & \\ & & & & & 2G \end{bmatrix}.$$

Similarly for the MH coupling term, we have

$$\begin{aligned} \mathbf{K}_{uP} &= -\frac{\partial R_M}{\partial \tilde{P}} = \frac{\partial \int_{\Omega} \mathbf{B}^T \boldsymbol{\sigma} d\Omega}{\partial \tilde{P}} \\ &= \int_{\Omega} \mathbf{B}^T \frac{\partial \boldsymbol{\sigma}}{\partial P} \frac{\partial P}{\partial \tilde{P}} d\Omega = \int_{\Omega} \mathbf{B}^T \mathbf{D}_{mh} \mathbf{N} d\Omega, \end{aligned} \tag{46}$$

where $\mathbf{D}_{mh} = [-b \ -b \ -b \ 0 \ 0 \ 0]^T$.

Recalling Eq. (39), the HM coupling Jacobians can be derived as

$$\begin{aligned} \mathbf{K}_{Pu} &= -\frac{\partial R_H}{\partial \tilde{\mathbf{u}}} = \frac{1}{\Delta t} \int_{\Omega} \mathbf{N}^T (\rho_{\text{surf}} C_n + \rho_f) \frac{\partial n}{\partial \tilde{\mathbf{u}}} d\Omega + \int_{\Omega} \mathbf{N}^T \rho_{\text{surf}} \dot{n} \frac{\partial C_n}{\partial n} \frac{\partial n}{\partial \tilde{\mathbf{u}}} d\Omega \\ &+ \int_{\Omega} \mathbf{N}^T \frac{\partial \rho_f}{\partial P} \frac{\partial P}{\partial \tilde{\mathbf{u}}} d\Omega + \int_{\Omega} \mathbf{N}^T C_n C_{\text{ads}} \frac{\partial n}{\partial \tilde{\mathbf{u}}} d\Omega + \frac{1}{\Delta t} \int_{\Omega} \mathbf{N}^T (\rho_{\text{surf}} a_s + \rho_f n) \frac{\partial \varepsilon}{\partial \tilde{\mathbf{u}}} d\Omega \\ &+ \int_{\Omega} \mathbf{N}^T \rho_{\text{surf}} \dot{\varepsilon} C_n \frac{\partial n}{\partial \tilde{\mathbf{u}}} d\Omega + \int_{\Omega} \mathbf{N}^T \rho_f \dot{\varepsilon} \frac{\partial n}{\partial \tilde{\mathbf{u}}} d\Omega. \end{aligned} \tag{47}$$

Considering

$$\frac{\partial n}{\partial \tilde{\mathbf{u}}} = \frac{\partial n}{\partial \phi} \frac{\partial \phi}{\partial \boldsymbol{\varepsilon}} \frac{\partial \boldsymbol{\varepsilon}}{\partial \mathbf{u}} \frac{\partial \mathbf{u}}{\partial \tilde{\mathbf{u}}} = J^{-1} \frac{\partial \phi}{\partial \boldsymbol{\varepsilon}} \nabla_s \mathbf{N} = J^{-1} \mathbf{D}_{nm} \mathbf{B},$$

where $\mathbf{D}_{nm} = [b \ b \ b \ 0 \ 0 \ 0]$, and $\boldsymbol{\varepsilon} = \nabla^T \mathbf{u} = \nabla^T \tilde{\mathbf{N}}\tilde{\mathbf{u}}$ with

$$\begin{aligned} \nabla^T \mathbf{N} &= \begin{bmatrix} \frac{\partial}{\partial x} & \frac{\partial}{\partial y} & \frac{\partial}{\partial z} \end{bmatrix} \begin{bmatrix} N_1 & N_2 & \dots & N_n \\ & N_1 & N_2 & \dots & N_n \\ & & N_1 & N_2 & \dots & N_n \end{bmatrix} \\ &= \begin{bmatrix} \frac{\partial N_1}{\partial x} & \frac{\partial N_1}{\partial y} & \frac{\partial N_1}{\partial z} & \frac{\partial N_2}{\partial x} & \frac{\partial N_2}{\partial y} & \frac{\partial N_2}{\partial z} & \dots & \frac{\partial N_n}{\partial x} & \frac{\partial N_n}{\partial y} & \frac{\partial N_n}{\partial z} \end{bmatrix}. \end{aligned}$$

Equation (47) can be rewritten as

Finally, the Jacobian for the H equation can be derived as

$$\mathbf{K}_{PP} = -\frac{\partial R_H}{\partial \bar{P}} = \frac{\partial \int_{\Omega} \mathbf{N}^T (\rho_{\text{surf}} C_n + \rho_f) \dot{n} d\Omega}{\partial \bar{P}} + \frac{\partial \int_{\Omega} \mathbf{N}^T \left(a_s \frac{\partial \rho_{\text{surf}}}{\partial P} + n \frac{\rho_f}{P} \right) \dot{P} d\Omega}{\partial \bar{P}} \tag{49}$$

$$+ \frac{\partial \int_{\Omega} \mathbf{N}^T (\rho_{\text{surf}} a_s + \rho_f n) \dot{\epsilon} d\Omega}{\partial \bar{P}} - \frac{\partial \int_{\Omega} (\nabla \mathbf{N})^T \mathbf{q}_f d\Omega}{\partial \bar{P}}.$$

According to Darcy’s law Eq. (23), we have

$$\frac{\partial \int_{\Omega} (\nabla \mathbf{N})^T \mathbf{q}_f d\Omega}{\partial \bar{P}} = - \int_{\Omega} (\nabla \mathbf{N})^T \frac{\rho_f k}{\mu_d} (\nabla \mathbf{N}) d\Omega. \tag{50}$$

$$\mathbf{J} = \begin{bmatrix} \frac{\partial x}{\partial \xi} & \frac{\partial y}{\partial \xi} & \frac{\partial z}{\partial \xi} \\ \frac{\partial x}{\partial \eta} & \frac{\partial y}{\partial \eta} & \frac{\partial z}{\partial \eta} \\ \frac{\partial x}{\partial \zeta} & \frac{\partial y}{\partial \zeta} & \frac{\partial z}{\partial \zeta} \end{bmatrix}.$$

For simplicity, the derivatives of $\partial n / \partial P$ are neglected in our implementation and fluid compressibility term ρ_f / P is treated as an independent variable with respect to \bar{P} . Supplementing these simplifications and Eq. (50) into Eq. (49) finally gives

The final expressions of residuals and Jacobians implemented in the UEL are summarized below. Note the surface flux terms in residuals Eqs. (38) and (39) are excluded in the final implementation because the natural boundary conditions of the M and H fields are applied on $\partial \Omega_t$ and $\partial \Omega_f^k$ in

$$\mathbf{K}_{PP} = \int_{\Omega} \mathbf{N}^T C_{\text{ads}} C_n \dot{n} \mathbf{N} d\Omega + \frac{1}{\Delta t} \int_{\Omega} \mathbf{N}^T \left(a_s C_{\text{ads}} + n \frac{\rho_f}{P} \right) \mathbf{N} d\Omega \tag{51}$$

$$+ \int_{\Omega} \mathbf{N}^T a_s \frac{\partial C_{\text{ads}}}{\partial P} \dot{P} \mathbf{N} d\Omega + \int_{\Omega} \mathbf{N}^T C_{\text{ads}} a_s \dot{\epsilon} \mathbf{N} d\Omega + \int_{\Omega} \mathbf{N}^T \frac{\rho_f}{P} n \dot{\epsilon} \mathbf{N} d\Omega + \int_{\Omega} (\nabla \mathbf{N})^T \frac{\rho_f k}{\mu_d} (\nabla \mathbf{N}) d\Omega.$$

Numerical Integration

The [R] and [K] matrixes contain several definite integral terms over the element. These integrals need to be evaluated by Gaussian quadrature after mapping them from Cartesian coordinates (x, y, z) to isoparametric coordinates (ξ, η, ζ). Targeting at the most generalized 3D analysis, an eight-node finite element (C3D8) interpolation is employed:

$$\int_{\Omega} f(x, y, z) d\Omega = \int_{-1}^1 \int_{-1}^1 \int_{-1}^1 \det \mathbf{J} f(\xi, \eta, \zeta) d\xi d\eta d\zeta \tag{52}$$

$$\approx \sum_{i=1}^2 \sum_{j=1}^2 \sum_{k=1}^2 W_i W_j W_k \det \mathbf{J} f(\xi, \eta, \zeta),$$

where J is also called Jacobian matrix in isoparametric mapping defined by

Eqs. (30) and (31) are handled by ABAQUS CAE.

$$R_M = - \sum_{i=1}^2 \sum_{j=1}^2 \sum_{k=1}^2 W_i W_j W_k \det \mathbf{J} \mathbf{B}^T(\xi_i, \eta_j, \zeta_k) \boldsymbol{\sigma}(\xi_i, \eta_j, \zeta_k), \tag{53}$$

$$R_H = - \sum_{i=1}^2 \sum_{j=1}^2 \sum_{k=1}^2 W_i W_j W_k \det \mathbf{J} \mathbf{N}^T(\xi_i, \eta_j, \zeta_k) (\rho_{\text{surf}} C_n + \rho_f) \dot{n}$$

$$- \sum_{i=1}^2 \sum_{j=1}^2 \sum_{k=1}^2 W_i W_j W_k \det \mathbf{J} \mathbf{N}^T \left(a_s C_{\text{ads}} + n \frac{\rho_f}{P} \right) \dot{P}(\xi_i, \eta_j, \zeta_k)$$

$$- \sum_{i=1}^2 \sum_{j=1}^2 \sum_{k=1}^2 W_i W_j W_k \det \mathbf{J} \mathbf{N}^T(\xi_i, \eta_j, \zeta_k) (\rho_{\text{surf}} a_s + \rho_f n) \dot{\epsilon}$$

$$+ \sum_{i=1}^2 \sum_{j=1}^2 \sum_{k=1}^2 W_i W_j W_k \det \mathbf{J} [\nabla \mathbf{N}(\xi_i, \eta_j, \zeta_k)]^T \mathbf{q}_f, \tag{54}$$

$$\mathbf{K}_{uu} = \sum_{i=1}^2 \sum_{j=1}^2 \sum_{k=1}^2 W_i W_j W_k \det \mathbf{J} \mathbf{B}^T(\xi_i, \eta_j, \zeta_k) [\mathbf{D}_{mm}] \mathbf{B}(\xi_i, \eta_j, \zeta_k), \tag{55}$$

$$\mathbf{K}_{uP} = \sum_{i=1}^2 \sum_{j=1}^2 \sum_{k=1}^2 W_i W_j W_k \det \mathbf{J} \mathbf{B}^T(\xi_i, \eta_j, \zeta_k) [\mathbf{D}_{mh}] \mathbf{N}(\xi_i, \eta_j, \zeta_k), \tag{56}$$

$$\begin{aligned}
 \mathbf{K}_{Pu} = & \frac{1}{\Delta t} \sum_{i=1}^2 \sum_{j=1}^2 \sum_{k=1}^2 W_i W_j W_k \det \mathbf{JN}^T(\xi_i, \eta_j, \zeta_k) (\rho_{\text{surf}} C_n + \rho_f n) J^{-1} \mathbf{D}_{nm} \mathbf{B}(\xi_i, \eta_j, \zeta_k) \\
 & + \sum_{i=1}^2 \sum_{j=1}^2 \sum_{k=1}^2 W_i W_j W_k \det \mathbf{JN}^T(\xi_i, \eta_j, \zeta_k) \rho_{\text{surf}} \dot{n} \frac{\partial C_n}{\partial n} J^{-1} \mathbf{D}_{nm} \mathbf{B}(\xi_i, \eta_j, \zeta_k) \\
 & + \sum_{i=1}^2 \sum_{j=1}^2 \sum_{k=1}^2 W_i W_j W_k \det \mathbf{JN}^T(\xi_i, \eta_j, \zeta_k) \left(\frac{\rho_f}{P} + C_n C_{\text{ads}} \right) J^{-1} \mathbf{D}_{nm} \mathbf{B}(\xi_i, \eta_j, \zeta_k) \dot{P}(\xi_i, \eta_j, \zeta_k) \\
 & + \frac{1}{\Delta t} \sum_{i=1}^2 \sum_{j=1}^2 \sum_{k=1}^2 W_i W_j W_k \det \mathbf{JN}^T(\xi_i, \eta_j, \zeta_k) (\rho_{\text{surf}} a_s + \rho_f n) \nabla^T \mathbf{N}(\xi_i, \eta_j, \zeta_k) \\
 & + \sum_{i=1}^2 \sum_{j=1}^2 \sum_{k=1}^2 W_i W_j W_k \det \mathbf{JN}^T(\xi_i, \eta_j, \zeta_k) \rho_{\text{surf}} \dot{\epsilon} C_n J^{-1} \mathbf{D}_{nm} \mathbf{B}(\xi_i, \eta_j, \zeta_k) \\
 & + \sum_{i=1}^2 \sum_{j=1}^2 \sum_{k=1}^2 W_i W_j W_k \det \mathbf{JN}^T(\xi_i, \eta_j, \zeta_k) \rho_f \dot{\epsilon} J^{-1} \mathbf{D}_{nm} \mathbf{B}(\xi_i, \eta_j, \zeta_k),
 \end{aligned} \tag{57}$$

$$\begin{aligned}
 \mathbf{K}_{PP} = & \sum_{i=1}^2 \sum_{j=1}^2 \sum_{k=1}^2 W_i W_j W_k \det \mathbf{JN}^T(\xi_i, \eta_j, \zeta_k) C_{\text{ads}} C_n \dot{n} \mathbf{N}(\xi_i, \eta_j, \zeta_k) \\
 & + \frac{1}{\Delta t} \sum_{i=1}^2 \sum_{j=1}^2 \sum_{k=1}^2 W_i W_j W_k \det \mathbf{JN}^T(\xi_i, \eta_j, \zeta_k) \left(a_s C_{\text{ads}} + n \frac{\rho_f}{P} \right) \mathbf{N}(\xi_i, \eta_j, \zeta_k) \\
 & + \sum_{i=1}^2 \sum_{j=1}^2 \sum_{k=1}^2 W_i W_j W_k \det \mathbf{JN}^T(\xi_i, \eta_j, \zeta_k) a_s \frac{\partial C_{\text{ads}}}{\partial P} \mathbf{N}(\xi_i, \eta_j, \zeta_k) \dot{P}(\xi_i, \eta_j, \zeta_k) \\
 & + \sum_{i=1}^2 \sum_{j=1}^2 \sum_{k=1}^2 W_i W_j W_k \det \mathbf{JN}^T(\xi_i, \eta_j, \zeta_k) C_{\text{ads}} a_s \dot{\epsilon} \mathbf{N}(\xi_i, \eta_j, \zeta_k) \\
 & + \sum_{i=1}^2 \sum_{j=1}^2 \sum_{k=1}^2 W_i W_j W_k \det \mathbf{JN}^T(\xi_i, \eta_j, \zeta_k) \frac{\rho_f}{P} n \dot{\epsilon} \mathbf{N}(\xi_i, \eta_j, \zeta_k) \\
 & + \frac{\rho_f k}{\mu_d} \sum_{i=1}^2 \sum_{j=1}^2 \sum_{k=1}^2 W_i W_j W_k \det \mathbf{J} [\nabla \mathbf{N}(\xi_i, \eta_j, \zeta_k)]^T [\nabla \mathbf{N}(\xi_i, \eta_j, \zeta_k)].
 \end{aligned} \tag{58}$$

Acknowledgements This research was supported by the U.S. Department of Energy through grant DE-NE0008771.

References

Bandyopadhyay K, Mallik J, Ghosh T (2020) Dependence of fluid flow on cleat aperture distribution and aperture-length scaling: a case study from Gondwana coal seams of Raniganj Formation, Eastern India. *Int J Coal Sci Technol* 7(1):133–146

Bangham D, Fakhoury N (1928) The expansion of charcoal accompanying sorption of gases and vapours. *Nature* 122:681

Bangham D, Razouk uR (1938) The saturation and immersion expansions and the heat of wetting. *Proc R Soc Lond A* 166:572–586

Brochard L, Vandamme M, Pellenq R-M (2012) Poromechanics of microporous media. *J Mech Phys Solids* 60:606–622

Chen Y, Liu D, Yao Y, Cai Y, Chen L (2015) Dynamic permeability change during coalbed methane production and its controlling factors. *J Nat Gas Sci Eng* 25:335–346

Clarkson CR, Pan Z, Palmer ID, Harpalani S (2010) Predicting sorption-induced strain and permeability increase with depletion for coalbed-methane reservoirs. *Spe J* 15:152–159

Coussy O (2004) *Poromechanics*. John Wiley & Sons Ltd, Chichester. <https://doi.org/10.1002/0470092718>

Coussy O (2010) *Mechanics and physics of porous solids*. John Wiley & Sons, Hoboken

Coussy O, Dormieux L, Detournay E (1998) From mixture theory to Biot’s approach for porous media. *Int J Solids Struct* 35:4619–4635

Cui X, Bustin RM (2005) Volumetric strain associated with methane desorption and its impact on coalbed gas production from deep coal seams. *Aapg Bull* 89:1181–1202

Dawson G, Esterle J (2010) Controls on coal cleat spacing. *Int J Coal Geol* 82:213–218

- DeHoff R (2006) Thermodynamics in materials science. CRC Press, Boca Raton
- Durucan S, Shi J-Q (2009) Improving the CO₂ well injectivity and enhanced coalbed methane production performance in coal seams. *Int J Coal Geol* 77:214–221
- Espinoza D, Vandamme M, Dangla P, Pereira JM, Vidal-Gilbert S (2013) A transverse isotropic model for microporous solids: application to coal matrix adsorption and swelling. *J Geophys Res Solid Earth* 118:6113–6123
- Fan L, Liu S (2018) Numerical prediction of in situ horizontal stress evolution in coalbed methane reservoirs by considering both poroelastic and sorption induced strain effects. *Int J Rock Mech Min Sci* 104:156–164
- Gilman A, Beckie R (2000) Flow of coal-bed methane to a gallery. *Transp Porous Media* 41:1–16
- Gor GY, Neimark AV (2010) Adsorption-induced deformation of mesoporous solids. *Langmuir* 26:13021–13027
- Gor GY, Neimark AV (2011) Adsorption-induced deformation of mesoporous solids: macroscopic approach and density functional theory. *Langmuir* 27:6926–6931
- Gor GY, Huber P, Bernstein N (2017) Adsorption-induced deformation of nanoporous materials—a review. *Appl Phys Rev* 4:011303
- Gu F, Chalaturnyk RJ (2006) Numerical simulation of stress and strain due to gas sorption/desorption and their effects on in situ permeability of coalbeds. *J Can Pet Technol* 45. <https://doi.org/10.2118/06-10-05>
- Harpalani S, Chen G (1995) Estimation of changes in fracture porosity of coal with gas emission. *Fuel* 74:1491–1498
- Harpalani S, Chen G (1997) Influence of gas production induced volumetric strain on permeability of coal. *Geotech Geol Eng* 15:303–325
- Harpalani S, Schraufnagel RA (1990) Shrinkage of coal matrix with release of gas and its impact on permeability of coal. *Fuel* 69:551–556
- Hol S, Spiers CJ (2012) Competition between adsorption-induced swelling and elastic compression of coal at CO₂ pressures up to 100MPa. *J Mech Phys Solids* 60:1862–1882
- Kozeny J (1927) Über kapillare Leitung des Wassers im Boden:(Aufstieg, Versickerung und Anwendung auf die Bewässerung). Hölder-Pichler-Tempsky, Vienna
- Levine JR (1996) Model study of the influence of matrix shrinkage on absolute permeability of coal bed reservoirs. *Geol Soc Lond Spec Publ* 109:197–212
- Liu S, Harpalani S (2013) Permeability prediction of coalbed methane reservoirs during primary depletion. *Int J Coal Geol* 113:1–10
- Liu S, Harpalani S (2014a) Compressibility of sorptive porous media: part 2 experimental study on coal compressibility of sorptive material, experimental study. *Aapg Bull* 98:1773–1788
- Liu S, Harpalani S (2014b) Evaluation of in situ stress changes with gas depletion of coalbed methane reservoirs. *J Geophys Res Solid Earth* 119:6263–6276
- Liu H-H, Rutqvist J (2010) A new coal-permeability model: internal swelling stress and fracture–matrix interaction. *Transp Porous Media* 82:157–171
- Liu J, Wang J, Chen Z, Wang S, Elsworth D, Jiang Y (2011) Impact of transition from local swelling to macro swelling on the evolution of coal permeability. *Int J Coal Geol* 88:31–40
- Liu J, Spiers CJ, Peach CJ, Vidal-Gilbert S (2016) Effect of lithostatic stress on methane sorption by coal: theory vs. experiment and implications for predicting in-situ coalbed methane content. *Int J Coal Geol* 167:48–64
- Liu S, Zhang R, Karpyn Z, Yoon H, Dewers T (2019) Investigation of accessible pore structure evolution under pressurization and adsorption for coal and shale using small-angle neutron scattering. *Energy Fuels* 33:837–847
- Liu A, Liu S, Wang G, Sang G (2020) Modeling of coal matrix apparent strains for sorbing gases using a transversely isotropic approach. *Rock Mech Rock Eng.* <https://doi.org/10.1007/s00603-020-02159-3>
- Ma Q, Harpalani S, Liu S (2011) A simplified permeability model for coalbed methane reservoirs based on matchstick strain and constant volume theory. *Int J Coal Geol* 85:43–48
- Mitra A, Harpalani S, Liu S (2012) Laboratory measurement and modeling of coal permeability with continued methane production: part 1—laboratory results. *Fuel* 94:110–116
- Nikoosokhan S, Vandamme M, Dangla P (2014) A poromechanical model for coal seams saturated with binary mixtures of CH₄ and CO₂. *J Mech Phys Solids* 71:97–111
- Palmer I (2009) Permeability changes in coal: analytical modeling. *Int J Coal Geol* 77:119–126
- Palmer I, Mansoori J (1996) How permeability depends on stress and pore pressure in coalbeds: a new model. In: SPE annual technical conference and exhibition, 1996. Society of Petroleum Engineers
- Pan Z, Connell LD (2012) Modelling permeability for coal reservoirs: a review of analytical models and testing data. *Int J Coal Geol* 92:1–44
- Pone JDN, Halleck PM, Mathews JP (2009) Sorption capacity and sorption kinetic measurements of CO₂ and CH₄ in confined and unconfined bituminous coal. *Energy Fuels* 23:4688–4695
- Ramandi HL, Mostaghimi P, Armstrong RT, Saadatfar M, Pinczewski WV (2016) Porosity and permeability characterization of coal: a micro-computed tomography study. *Int J Coal Geol* 154:57–68
- Ravikovitch PI, Neimark AV (2006) Density functional theory model of adsorption deformation. *Langmuir* 22:10864–10868
- Reeves SR (2001) Geological sequestration of CO₂ in deep, unminable coalbeds: an integrated research and commercial-scale field demonstration project. In: SPE annual technical conference and exhibition, 2001. Society of Petroleum Engineers
- Reiss LH (1980) The reservoir engineering aspects of fractured formations, vol 3. Editions Technip, Paris
- Sarkar S, Toksoz MN, Burns DR (2004) Fluid flow modeling in fractures. Massachusetts Institute of Technology. Earth Resources Laboratory
- Seidle JR, Huiitt L (1996) Experimental measurement of coal matrix shrinkage due to gas desorption and implications for cleat permeability increases. In: International meeting on petroleum engineering, 1995. Society of Petroleum Engineers
- Seidle J, Jeansonne M, Erickson D (1992) Application of matchstick geometry to stress dependent permeability in coals. In: SPE rocky mountain regional meeting, 1992. Society of Petroleum Engineers
- Shi J, Durucan S (2004) Drawdown induced changes in permeability of coalbeds: a new interpretation of the reservoir response to primary recovery. *Transp Porous Media* 56:1–16
- Shi J-Q, Durucan S (2005) A model for changes in coalbed permeability during primary and enhanced methane recovery. *SPE Reserv Eval Eng* 8:291–299
- Shi J-Q, Pan Z, Durucan S (2014) Analytical models for coal permeability changes during coalbed methane recovery: model comparison and performance evaluation. *Int J Coal Geol* 136:17–24
- Shovkun I, Espinoza DN (2017) Coupled fluid flow-geomechanics simulation in stress-sensitive coal and shale reservoirs: impact of desorption-induced stresses, shear failure, and fines migration. *Fuel* 195:260–272
- Shuttleworth R (1950) The surface tension of solids. *Proc Phys Soc Sect A* 63:444
- Vandamme M, Brochard L, Lecampion B, Coussy O (2010) Adsorption and strain: the CO₂-induced swelling of coal. *J Mech Phys Solids* 58:1489–1505
- Wang Y, Liu S (2016) Estimation of pressure-dependent diffusive permeability of coal using methane diffusion coefficient: laboratory measurements and modeling. *Energy Fuels* 30:8968–8976

- Wang S, Elsworth D, Liu J (2013) Permeability evolution during progressive deformation of intact coal and implications for instability in underground coal seams. *Int J Rock Mech Min Sci* 58:34–45
- Wang K, Zang J, Wang G, Zhou A (2014) Anisotropic permeability evolution of coal with effective stress variation and gas sorption: model development and analysis. *Int J Coal Geol* 130:53–65
- Zhang Y (2018) Mechanics of adsorption–deformation coupling in porous media. *J Mech Phys Solids* 114:31–54
- Zhang Y, Lebedev M, Sarmadivaleh M, Barifcani A, Rahman T, Iglauer S (2016) Swelling effect on coal micro structure and associated permeability reduction. *Fuel* 182:568–576
- Zhao Y, Hu Y, Wei J, Yang D (2003) The experimental approach to effective stress law of coal mass by effect of methane. *Transp Porous Media* 53:235–244

Publisher's Note Springer Nature remains neutral with regard to jurisdictional claims in published maps and institutional affiliations.